



INDIAN INSTITUTE OF TECHNOLOGY
BOMBAY

BACHELOR THESIS

Automation and Control of a Superconducting Quantum Processor

Author: Aneesh Anand KAMAT

Supervisor: Dr. Rajamani VIJAYARAGHAVAN

Co-Supervisor: Dr. Suddhasatta MAHAPATRA

*A thesis submitted in fulfillment of the requirements
for the degree of Bachelor of Technology*

in the

Department of Physics
IIT Bombay

for research conducted at the

Quantum Measurement and Control Laboratory
Tata Institute of Fundamental Research (TIFR), Mumbai

November 27, 2023

Declaration of Authorship

I, Aneesh Anand KAMAT, declare that this thesis titled, “Automation and Control of a Superconducting Quantum Processor” and the work presented in it are my own. I confirm that:

- This work was done wholly or mainly while in candidature for a research degree at this University.
- Where any part of this thesis has previously been submitted for a degree or any other qualification at this University or any other institution, this has been clearly stated.
- Where I have consulted the published work of others, this is always clearly attributed.
- Where I have quoted from the work of others, the source is always given. With the exception of such quotations, this thesis is entirely my own work.
- I have acknowledged all main sources of help.
- Where the thesis is based on work done by myself jointly with others, I have made clear exactly what was done by others and what I have contributed myself.

Signed:

Date:

Abstract

Aneesh Anand KAMAT

Automation and Control of a Superconducting Quantum Processor

This thesis outlines a protocol to tune up a superconducting quantum processor in an automated manner with minimal human operator input. The work conducted in this thesis was carried out on fixed-frequency transmon qubits, as part of a collaborative effort between TIFR, DRDO and TCS to develop India's first quantum computer, a 7-qubit processor accessible to scientists via cloud in a manner akin to IBM's extremely successful IBMQ platform. Such an effort necessitates a capability to characterize, calibrate and control qubits in an automated manner, while also executing a periodic re-tuning of critical configuration parameters, to maximise the up-time of the quantum processor, and minimize human operator resources.

We present an automated spectroscopy code to characterize the qubits using microwave control lines with a custom SNR detector that allows efficient ensemble averaging. We demonstrate the ALLXY error diagnostic tool to benchmark gate performance and measure robustness. This is extended to an experimental calibration of DRAG pulses to address the issue of state leakage out of the qubit computational basis. We implement an autonomous closed-loop amplitude calibration of π and $\pi/2$ pulses using the ORBIT fidelity measure, achieving Randomized Benchmarking fidelities at par with manually calibrated pulses using the resource-expensive Power Rabi experiment.

All the above additions to the experimental suite for qubit tune-up are developed in the Quantum Universal Assembly (QUA) language in a scalable manner that can simultaneously extend to all the qubits in the quantum processor unit. They are integrated with industry-standard techniques such as Rabi, Ramsey, Randomized Benchmarking and Coherence experiments to demonstrate cool-down to coherence with minimal human operator oversight.

Acknowledgements

I am extremely grateful to my supervisor Rajamani Vijayaraghavan for allowing me the opportunity to join his group, first as a research intern and then as a project student. The last six months at the Quantum Measurement and Control (QuMaC) lab at TIFR Mumbai have been pivotal in my decision to continue pursuing research.

In our first discussion regarding possible problem statements I could tackle, Vijay brought up the need to automate and optimally control our qubits to address the extensive human resource requirements that everyday operations required at the time. I recall being simultaneously overawed, anxious and confident when I learnt that I would be entrusted with a key role in the DRDO-TCS-TIFR project to develop India's first quantum computer. It didn't help when Vijay reiterated that if I took this up, I would need to take up the sole responsibility for its completion and no one else would be actively working on it. Looking back, I am beyond grateful for his trust in me. I take immense pride in seeing my work contribute significantly to a watershed moment for our national quantum computing ambitions.

Vijay has put together a group containing some of the smartest minds in the country, but just as importantly, some of the nicest humans I have ever met. My experience with the entire QuMaC group has been consistently inspiring. Many many thanks are due to Jay Deshmukh and Binoy Nambiar for their mentorship, friendship and innate ability to get through complicated challenges with a smile on their faces. Our conversations spanning physics, philosophy and pop culture are a cherished memory. Jay taught me everything I know about superconducting qubits and Binoy has been the resident control theory expert in whom I always had a willing soundboard to bounce new ideas off. Their organizational skills, attention to detail and meticulous management of responsibilities have set a standard I aspire to realize.

I am grateful, also, to the larger QuMaC family - Gaurav (Agarwal), Sri-jita, Kishor, Gaurav (Bothara), Anirban, Madhavi, Meghan and Lakshay - who have always made me feel welcome and indulged my never-ending curiosity in their work. Thank you for many memories, uncountable quantum computing and physics discussions, and loads of fun.

Contents

Declaration of Authorship	i
Abstract	ii
Acknowledgements	iii
List of Figures	vi
List of Abbreviations	vii
1 Introduction	1
1.1 Engineering Quantum Circuits	1
1.1.1 Qubits from Harmonic Oscillators	1
1.1.2 Coupling to the qubit	2
1.2 Noise and Decoherence	3
1.2.1 Types of noise	4
1.2.2 Modeling noise and decoherence	4
1.3 Characterizing coherence of qubits	6
1.3.1 Longitudinal relaxation	6
1.3.2 Pure dephasing	6
1.3.3 Transverse relaxation	7
1.4 Qubit Control	8
1.4.1 Capacitive coupling for X and Y control	9
1.4.2 Virtual Z gate	11
1.4.3 The DRAG scheme	11
1.5 Qubit Readout	13
1.5.1 Dispersive readout	13
1.5.2 Measuring resonator amplitude and phase	13
2 Tuning up a Superconducting Qubit	17
2.1 Mixer Calibration	17
2.2 Time of Flight Calibration	17
2.3 Readout Resonator Spectroscopy	17
2.4 Qubit Spectroscopy	18
2.5 Time Domain Rabi	20
2.6 IQ Calibration	20
2.7 Power Rabi Calibration	22
2.8 Time Domain Ramsey	26
2.9 Interleaved Coherence	27
2.10 Randomized Benchmarking	27

2.10.1	Simultaneous Randomized Benchmarking	28
3	Experimental Results	30
3.1	AutoSpectroscopy	30
3.2	ALLXY Pulse Calibration	31
3.2.1	Simultaneous ALLXY	33
3.2.2	DRAG parameter calibration	33
3.3	Closed-Loop Amplitude Calibration	35
3.3.1	Ad-HOC protocol	35
3.3.2	Nelder-Mead Algorithm	37
3.3.3	ORBIT figure of merit	38
3.3.4	Automatic Amplitude Calibration	38
3.3.5	ORBIT for DRAG and amplitude calibration	38
3.4	Automated Single Qubit Tune-Up Protocol	40
3.4.1	Results on a Tantalum Transmon	40
4	Conclusion	45
4.1	A Brief Summary	45
4.2	Future Avenues	45
4.2.1	Multi-qubit operations	45
4.2.2	Robust Single Qubit Pulses	45
	Bibliography	46

List of Figures

1.1	Quantum Harmonic Oscillator and Transmon	2
1.2	Bloch sphere.	5
1.3	T1 and Hahn Echo Experiments.	7
1.4	Ramsey interferometry experiment.	8
1.5	A typical qubit drive setup.	10
1.6	DRAG modulation pulse.	12
1.7	The DRAG scheme.	15
1.8	Dispersive Qubit Readout	16
2.1	Time of Flight calibration of ADC offsets.	18
2.2	Cavity Spectroscopy of Readout Resonator	19
2.3	An ideal qubit spectroscopy scan.	20
2.4	Qubit spectroscopy example	21
2.5	Well resolved qubit frequency	22
2.6	Rabi oscillations	23
2.7	IQ calibration	24
2.8	Power Rabi experiment.	25
2.9	Ramsey oscillations.	26
2.10	Coherence experiment for a qubit.	27
2.11	Single qubit standard RB.	28
2.12	Simultaneous RB on a pair of qubits.	29
3.1	Successive stages of the AutoSpectroscopy code.	32
3.2	ALLXY pulse sequence on a real qubit	34
3.3	Closed loop calibration of DRAG parameter	35
3.4	Fidelity improvement using DRAG pulses	36
3.5	The Ad-HOC protocol	37
3.6	Closed-loop calibration using ORBIT.	39
3.7	Auto-tuneup Broad sweep spectroscopy of qubit	40
3.8	Auto-tuneup Fine sweep spectroscopy of qubit	42
3.9	Auto-tuneup Time Rabi	43
3.10	Auto-tuneup Time Ramsey	43
3.11	Auto-tuneup ORBIT	44
3.12	Auto-tuneup Coherence and RB	44

List of Abbreviations

QUA	Quantum Universal Assembly
DOF	Degrees of Freedom
AHO	Anharmonic Oscillator
QHO	Quantum Harmonic Oscillator
JJ	Josephson Junctions
TLS	Two Level Systems
DRAG	Derivative Removal by Adiabatic Gate
cQED	cavity Quantum Electrodynamics
RWA	Rotating Wave Approximation
AWG	Arbitrary Waveform Generator
IQ	In-phase and Quadrature
LO	Local Oscillator
SNR	Signal to Noise Ratio
RO	Readout
SSB-SC	Single-sideband modulation with Suppressed Carrier
RF	Radio Frequency
DSP	Digital Signal Processing
TOF	Time of Flight
ADC	Analog to Digital Converter
DAC	Digital to Analog Converter
IF	Intermediate Frequency
RB	Randomized Benchmarking
QPU	Quantum Processing Unit
FWHM	Full Width Half Maxima
ORBIT	Optimized Randomized Benchmarking for Immediate Tune-up
Ad-HOC	Adaptation by Hybrid Optimal Control
OCT	Optimal Control Theory
PPU	Pulse Processing Unit

Dedicated to my parents and
grandparents, an enduring
source of love and inspiration.

1 Introduction

In this chapter, we introduce the fundamental concepts required to contextualise the work conducted in this thesis. The platform of superconducting qubits is motivated and the challenges in operating it are outlined. We follow the excellent reference of (Krantz et al., 2019).

1.1 Engineering Quantum Circuits

One of the most promising architectures for realizing practical quantum computers uses superconducting qubits controlled by microwave signals. These may come in various designs, the most ubiquitous being the fixed-frequency transmon for its simplicity and effectiveness. Here, information is stored in quantum degrees of freedom (DOFs) of nanofabricated anharmonic oscillators (AHOs) constructed from superconducting circuit elements. In contrast to other candidate platforms where the quantum information is naturally encoded in microscopic quantum systems, superconducting qubits are macroscopic in size and lithographically defined.

1.1.1 Qubits from Harmonic Oscillators

As the energy spectrum in a superconducting qubit is governed by circuit element parameters, they can be configured to exhibit "atom-like" energy spectra as desired. The dynamics of a superconducting qubit circuit can be understood by analysing a quantum harmonic oscillator (QHO) but introducing an anharmonicity (or non-linearity) so that transitions between states can be individually addressable.

In practice, the extent of non-linearity sets a limit on how short the pulses used to drive a transition can be. This nonlinearity is introduced using the Josephson junction (JJ) - a nonlinear, dissipation-less circuit element replacing the linear inductor in an LC circuit representation of a QHO. This allows us to identify a uniquely addressable quantum two-level system (TLS).

If excitation to higher non-computational states is suppressed over the gate operations, either due to a large enough anharmonicity or robust control techniques such as the derivative reduction by adiabatic gate (DRAG) pulse, see 3, we can effectively treat the AHO as a quantum TLS with a Hamiltonian

$$H = \omega_q \frac{\sigma_z}{2},$$

where σ_z is the Pauli-z operator. It is important however to remember that higher levels physically exist and influence system dynamics and control.

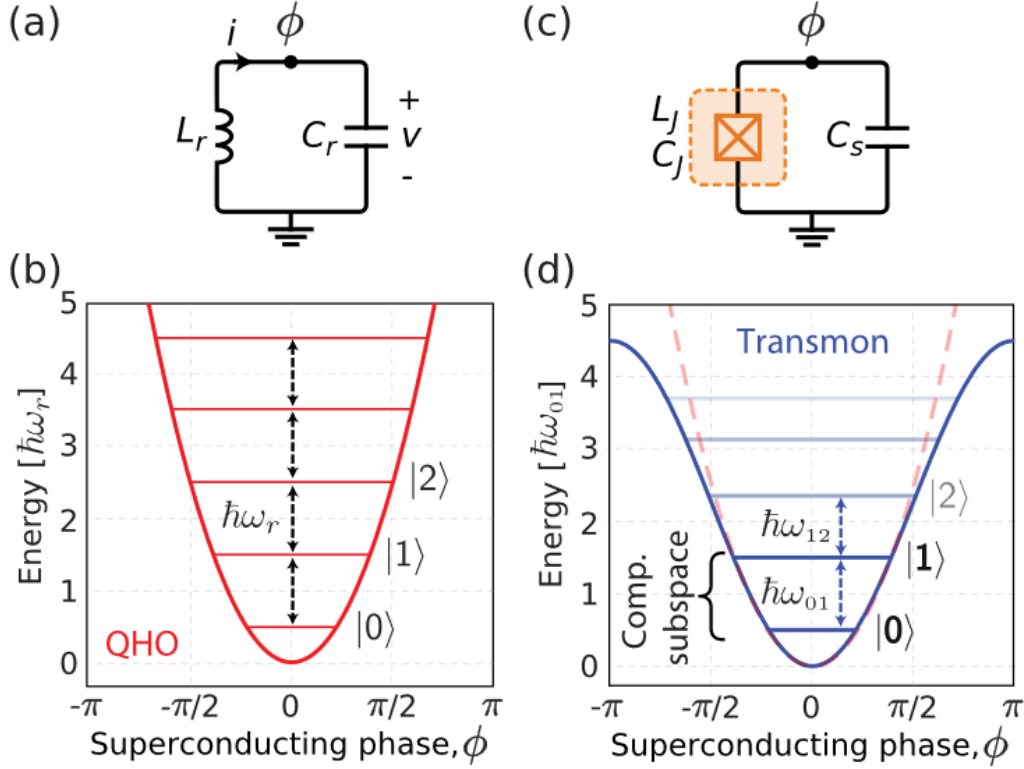


FIGURE 1.1: (a) QHO realized as an LC oscillator circuit, (b) Equidistantly spaced energy levels of QHO, (c) Josephson qubit circuit, (d) The Josephson inductance reshapes the quadratic energy potential (dashed red) into sinusoidal (solid blue) with non-equidistant energy levels. Taken from Krantz et al., 2019.

1.1.2 Coupling to the qubit

To generate entanglement between individual quantum systems it is necessary to engineer an interaction Hamiltonian connecting their degrees of freedom. Physical coupling mechanisms can be either capacitive or inductive and the Hamiltonian of two coupled systems takes a generic form

$$H = H_1 + H_2 + H_{int},$$

where H_1 and H_2 denote the Hamiltonians of the individual quantum systems and the last term H_{int} is the interaction Hamiltonian coupling the variables of both systems. For superconducting circuits, the coupling is physically realized using either an electric or magnetic field (or a combination thereof).

The effect of coupling on system dynamics is governed by its form as represented in the eigenbasis of the individual systems i.e., how H_{int} appears in the representation spanned by the eigenbasis of $H_1 \otimes H_2$. In the TLS regime, the Hamiltonian of two spins coupled by an exchange interaction is given by

$$H = \sum_{i \in 1,2} \frac{1}{2} \omega_i \sigma_{z,i} + g \sigma_{x,1} \sigma_{x,2}.$$

Such a coupling is called "transverse" because the coupling Hamiltonian has nonzero matrix elements only at off-diagonal positions with respect to both oscillators. The interaction term is more commonly expressed as $\sigma_x \sigma_x$ instead of $\sigma_y \sigma_y$, the choice is arbitrary and does not change the dynamics, but when both capacitive and inductive couplings are presented we may need both forms of transverse couplings.

Transverse coupling can be engineered between a qubit and a harmonic oscillator in which case the Hamiltonian becomes

$$H = \frac{1}{2} \omega_q \sigma_z + \omega_r a^\dagger a + g(\sigma_+ a + \sigma_- a^\dagger),$$

where ω_q and ω_r are the qubit and resonator frequencies, and $\sigma_+ = |0\rangle\langle 1|$ and $\sigma_- = |1\rangle\langle 0|$ describe the process of exciting and de-exciting the qubit, respectively, we here assume coupling in the dispersive limit i.e., $g \ll \omega_q, \omega_r$, and thus ignore the double (de)excitation terms proportional to $\sigma_+ a^\dagger$ and $\sigma_- a$ which under typical operations oscillate fast enough to average to zero.

Such a Hamiltonian is the standard model describing how a two-level atom interacts with a resonant cavity that houses it - such a structure is known as cavity quantum electrodynamics (cQED), and has been extended to the circuit version here. The 3D transmons used for the work in this thesis consist of a 2D transmon coupled to a 3D cavity.

1.2 Noise and Decoherence

The operational fidelity of qubits can be affected by random, uncontrollable physical processes in the control and measurement equipment, or the local environment surrounding the processor. Such sources of noise induce decoherence which can be mitigated to some extent using coherent control techniques.

In a closed system, the dynamical evolution of a qubit state is deterministic. If the starting state and the Hamiltonian governing the evolution are known then we can predict the state of the qubit at an arbitrary time. In open systems however the qubit can interact with its environment, this is noise, and the qubit state looks less like our predicted state as time progresses and eventually, the state is lost.

1.2.1 Types of noise

Noise can be systematic or stochastic. The former, systematic noise, arises from a process that can be traced back to a fixed control or readout error i.e., we apply a microwave pulse to the qubit to impart a 180° rotation. If the control field is not tuned properly, it is possible that the pulse slightly over-rotates or under-rotates the qubit by a fixed amount. Such an error is "systematic" and by careful calibration of pulses, it can be corrected.

The latter, stochastic noise, arises from random fluctuations of parameters coupled to our qubit i.e., the thermal noise of a 50Ω resistor in the control lines leading to the qubit will have Johnson noise - voltage and current fluctuations - with a noise power that is proportional to both temperature and bandwidth. Stochastic noise can also be introduced by randomly fluctuating electromagnetic fields in the local qubit environment - on the metal surface, substrate surface or at their interface - which can couple to the qubit. Such unknown and uncontrolled fluctuations of one or more qubit parameters lead to qubit decoherence.

1.2.2 Modeling noise and decoherence

The qubit response to noise depends on how the noise couples to it - either through a longitudinal or transverse coupling with reference to the qubit quantization axis. This can be visualized using the "Bloch Sphere" picture of the qubit state, see Fig 1.2. This is a unit sphere used to describe the quantum state of a two-level system (qubit). The "Bloch vector" represents the state $|\psi\rangle = \alpha|0\rangle + \beta|1\rangle$. By convention, the north pole represents state $|0\rangle$ and the south pole state $|1\rangle$. For pure quantum states such as $|\psi\rangle$, the Bloch vector has unit length, $|\alpha|^2 + |\beta|^2 = 1$, and joins the centre of the sphere to a point on the surface.

The z -axis connecting the north and south poles is called the "longitudinal axis" as it represents the "qubit quantization axis" for states $|0\rangle$ and $|1\rangle$ in the qubit eigenbasis. The $x - y$ plane is the "transverse plane" with "transverse axes" x and y . In Cartesian coordinates, the unit Bloch vector $\vec{a} = (\sin \theta \cos \phi, \sin \theta \sin \phi, \cos \theta)$ is characterized using the polar angle $0 \leq \theta \leq \pi$ and the azimuthal angle $0 \leq \phi < 2\pi$. Following convention, state $|0\rangle$ at the north pole is associated with $+1$, and state $|1\rangle$ (the south pole) with -1 . An arbitrary quantum state can now be represented as

$$|\psi\rangle = \alpha|0\rangle + \beta|1\rangle = \cos \frac{\theta}{2}|0\rangle + e^{i\phi} \sin \frac{\theta}{2}|1\rangle.$$

If state $|1\rangle$ has higher energy than state $|0\rangle$ (the norm in superconducting qubits), then in a stationary frame the Bloch vector precesses around the z -axis at the qubit frequency $(E_1 - E_0)/\hbar$, and the Bloch vector is stationary on the Bloch sphere in the "rotating frame picture" - a reference frame where the x and y -axes also rotate around the z -axis at the qubit frequency.

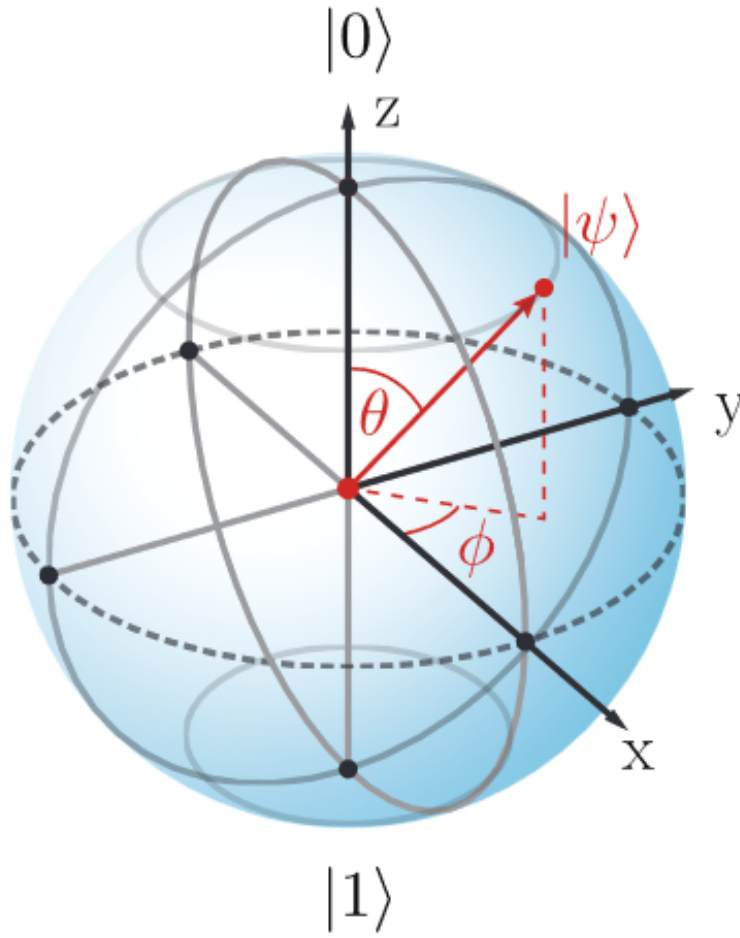


FIGURE 1.2: The Bloch sphere.

The impact of noise on the qubit can be visualized on the Bloch sphere where noise sources weakly coupled to the qubits have short correlation times with respect to the system dynamics. In this case, the relaxation processes are characterized by two rates,

$$\text{longitudinal relaxation rate: } \Gamma_1 \equiv \frac{1}{T_1},$$

$$\text{transverse relaxation rate: } \Gamma_2 \equiv \frac{1}{T_2} = \frac{\Gamma_1}{2} + \Gamma_\phi,$$

which contains the pure dephasing rate Γ_ϕ . Note that the definition of Γ_2 as a sum of rates presumes that the individual decay functions are exponential, which is true for Lorentzian noise spectra (centred at $\omega = 0$).

1.3 Characterizing coherence of qubits

1.3.1 Longitudinal relaxation

The longitudinal relaxation rate Γ_1 describes the depolarization along the qubit quantization axis and is often referred to as "energy decay" or "energy relaxation". A qubit with polarization $p = 1$ is entirely in the ground state ($|0\rangle$) at the north pole, $p = -1$ is entirely in the excited state ($|1\rangle$) at the south pole, and $p = 0$ is a completely depolarized mixed state at the centre of the Bloch sphere.

Longitudinal relaxation is caused by "transverse noise" via the x or y -axis - consistent with the intuition requiring off-diagonal elements of an interaction Hamiltonian to connect and drive transitions between states $|0\rangle$ and $|1\rangle$. Depolarization occurs due to the exchange of energy with an environment, leading to both an "up transition rate" $\Gamma_{1\uparrow}$ (excitation from $|0\rangle$ to $|1\rangle$), and a "down transition rate" $\Gamma_{1\downarrow}$ (relaxation from $|1\rangle$ to $|0\rangle$), together giving

$$\Gamma_1 \equiv \frac{1}{T_1} = \Gamma_{1\downarrow} + \Gamma_{1\uparrow}.$$

T_1 is the $1/e$ decay time in the exponential decay function and is the characteristic time scale over which the qubit population will relax to its steady-state value. This steady-state value is generally the ground state for superconducting qubits, due to Boltzmann statistics and operating conditions which exponentially suppress the up-rate $\Gamma_{1\uparrow}$.

To measure T_1 , the qubit is prepared in its excited state using an X_π -pulse and then left to spontaneously decay to the ground state for a time τ , after which the qubit is measured. A single measurement will project the quantum state into either state $|0\rangle$ or state $|1\rangle$, with probabilities that correspond to the qubit polarization. To make an estimate of this polarization, we must identically prepare the qubit and repeat the experiment many times to obtain an ensemble average. The resulting exponential decay has a characteristic time T_1 , see Fig 1.3.

1.3.2 Pure dephasing

The "pure dephasing" rate Γ_ϕ describes depolarization in the x - y plane of the Bloch sphere. It is referred to as "pure dephasing" to distinguish it from other phase-breaking processes such as energy excitation or relaxation. It is caused by "longitudinal noise" that couples to the qubit via the z -axis. Such longitudinal noise causes the qubit frequency ω_q to fluctuate, such that it is no longer equal to the rotating frame frequency ω_d , and causes the Bloch vector to process forwards or backwards in the rotating frame.

Intuitively, we can imagine preparing several identical instances of the Bloch vector along the x -axis. For each instance, the stochastic fluctuations of

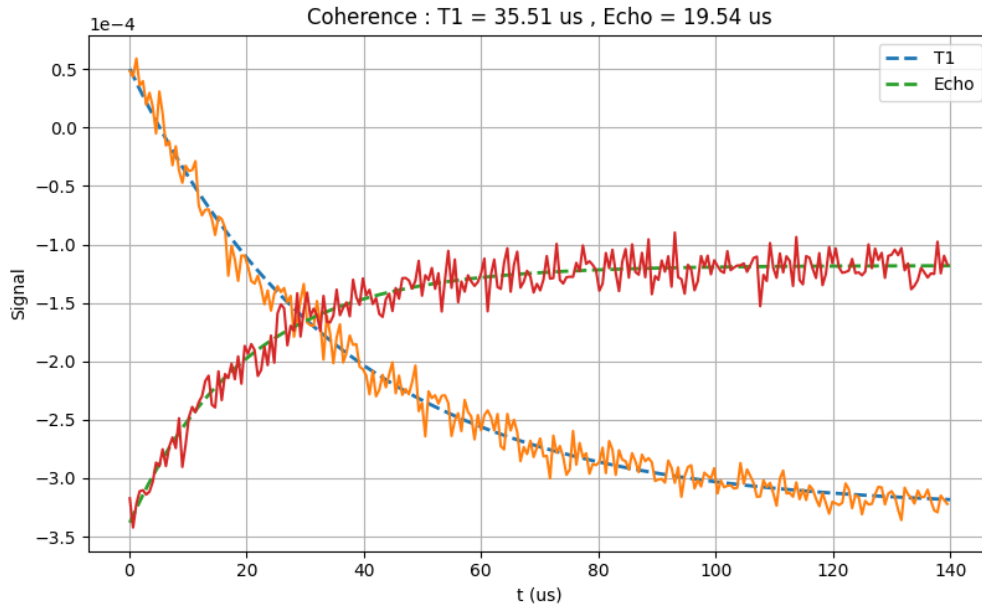


FIGURE 1.3: Longitudinal (energy) relaxation measurement using the T1 experiment. Transverse relaxation (decoherence) measurement via a Hahn echo experiment.

the qubit frequency will result in a different precession frequency, resulting in a net fanout of the Bloch vector in the x - y plane. This eventually leads to a complete depolarization of the azimuthal angle ϕ . This stochastic effect is captured in the transverse relaxation rate Γ_2 ; it is "not" the deterministic term $\exp(\pm i\delta\omega t)$ which is the intentional detuning of the qubit reference frame.

1.3.3 Transverse relaxation

The transverse relaxation rate $\Gamma_2 = \Gamma_1/2 + \Gamma_\phi$ describes the loss of coherence of a superposition state. Decoherence is caused in part by longitudinal noise, which fluctuates the qubit frequency and causes pure dephasing Γ_ϕ as discussed earlier. It is also caused by transverse noise, which leads to energy relaxation of the excited-state component of the superposition state at a rate Γ_1 .

Such a relaxation event is also a phase-breaking process as once it occurs, the Bloch vector points to the north pole, $|0\rangle$, and there is no knowledge of which direction it *had* been pointing along the equator; the relative phase of the superposition state is lost.

Transverse relaxation T_2 can be measured using Ramsey interferometry - the protocol positions the Bloch vector on the equator using an $X_{\pi/2}$ -pulse. Typically, the carrier frequency of the pulse is slightly detuned from the qubit frequency by an amount $\delta\omega$. As a result, the Bloch vector precesses around the z -axis at a rate $\delta\omega$, which causes the resulting Ramsey measurement to

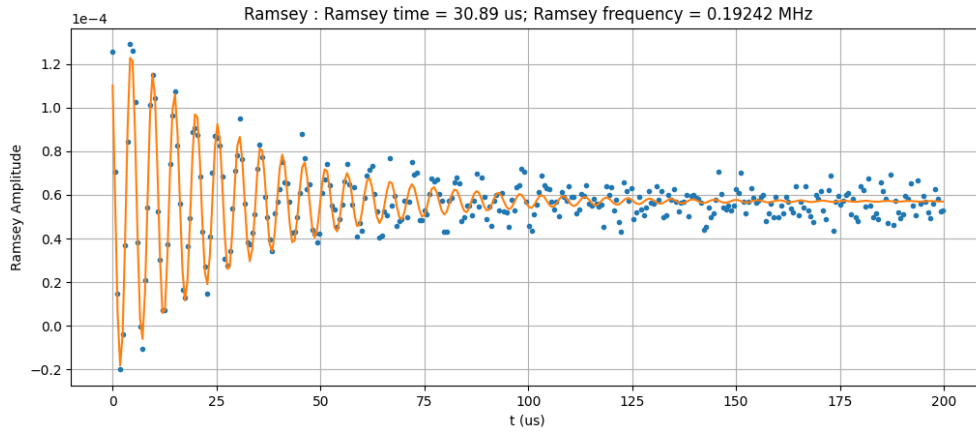


FIGURE 1.4: (b) Transverse relaxation (decoherence) measurement via Ramsey interferometry.

oscillate and ease subsequent analysis. After processing for a time τ , a second $X_{\pi/2}$ -pulse projects the Bloch vector back onto the z -axis.

The qubit is prepared on the equator using an $X_{\pi/2}$ -pulse, intentionally detuned from the qubit which causes the Bloch vector to process in the rotating frame around the z -axis. After a time τ , a second $X_{\pi/2}$ -pulse projects the Bloch vector back onto the z -axis, mapping its former position on the equator to a position on the z -axis. The oscillations decay with an approximately exponential decay function with characteristic time T_2^* , see Fig 1.4. The "*" indicates that the Ramsey experiment is sensitive to "inhomogeneous broadening" - quasistatic, low-frequency fluctuations that are constant within one experimental trial, but vary from trial to trial.

The Hahn echo experiment is less sensitive to quasistatic noise - by placing a Y_{π} -pulse at the centre of the Ramsey interferometry experiment, the quasistatic contributions to dephasing can be "refocused", and thus less sensitive to inhomogeneous broadening mechanisms. The resulting decay function is essentially exponential with time T_{2E} , see Fig 1.3. With the known T_1 and T_2 times, one can infer the pure dephasing time T_{ϕ} provided the decay functions are exponential.

1.4 Qubit Control

In this section, we will introduce how superconducting qubits can be manipulated to implement quantum algorithms. Quantum logic can be performed by a small set of single-qubit and two-qubit gates. Single-qubit operations translate an arbitrary quantum state from one point on the Bloch sphere to another by rotating the Bloch vector (spin) by a certain angle about a particular axis.

The "identity gate" performs no rotation on the state of the qubit, this is a two-by-two identity matrix. The X-gate performs a π rotation about the x -axis. Similarly, Y-gate and Z-gate perform a π rotation about the y -axis and the z -axis, respectively. Capacitive coupling is used to address fixed-frequency transmon qubits. The capacitive coupling between a resonator (or a feedline) and the superconducting qubit dipole field allows for microwave control to implement single qubit rotations.

1.4.1 Capacitive coupling for X and Y control

Consider coupling a superconducting qubit to a microwave source (also called a "qubit drive"). The capacitive coupling can be used for X and Y control with the circuit Hamiltonian for weak coupling given by

$$H = \underbrace{-\frac{\omega_q}{2}\sigma_z}_{H_0} + \underbrace{\Omega V_d(t)\sigma_y}_{H_d}.$$

We can move into a frame rotating with the qubit at frequency ω_q (the "rotating frame" or "interaction frame"), in which the form of H_d is

$$\tilde{H}_d = \Omega V_d(t) (\cos(\omega_q t)\sigma_y - \sin(\omega_q t)\sigma_x).$$

We can in general assume that the time-dependent part of the voltage ($V_d(t) = V_0 v(t)$) has the generic form

$$v(t) = s(t) \sin(\omega_d t + \phi) = s(t) (\cos(\phi) \sin(\omega_d t) + \sin(\phi) \cos(\omega_d t)),$$

where $s(t)$ is a dimensionless envelope function so that the amplitude of the drive is set by $V_0 s(t)$. We adopt the definitions

$$I = \cos(\phi) \text{ (the 'in-phase' component),}$$

$$Q = \sin(\phi) \text{ (the 'out-of-phase' component),}$$

the driving Hamiltonian in the rotating frame takes the form

$$\tilde{H}_d = \Omega V_0 s(t) (I \sin(\omega_d t) - Q \cos(\omega_d t)) \times (\cos(\omega_q t)\sigma_y - \sin(\omega_q t)\sigma_x).$$

In the rotating wave approximation (RWA), where we drop fast rotating terms that average to zero (i.e., terms with $\omega_q + \omega_d$) we have

$$\tilde{H}_d = -\frac{\Omega}{2} V_0 s(t) \begin{pmatrix} 0 & e^{i(\delta\omega t + \phi)} \\ e^{-i(\delta\omega t + \phi)} & 0 \end{pmatrix}.$$

This is a powerful representation to understand single-qubit gates in superconducting qubits. Assume we apply a pulse at the qubit frequency such that $\delta\omega = \omega_q - \omega_d = 0$, then

$$\tilde{H}_d = -\frac{\Omega}{2} V_0 s(t) (I\sigma_x + Q\sigma_y),$$

showing that an "in-phase" pulse ($\phi = 0$, i.e., the I -component) corresponds to rotations about the x -axis, while an "out-of-phase" pulse ($\phi = \pi/2$, i.e., the Q -component) corresponds to rotations about the y -axis. We define the shorthand

$$\Theta(t) = -\Omega V_0 \int_0^t s(t') dt',$$

which is the angle by which a state is rotated given the capacitive couplings, the impedance of the circuit, the magnitude V_0 , and the waveform envelope $s(t)$.

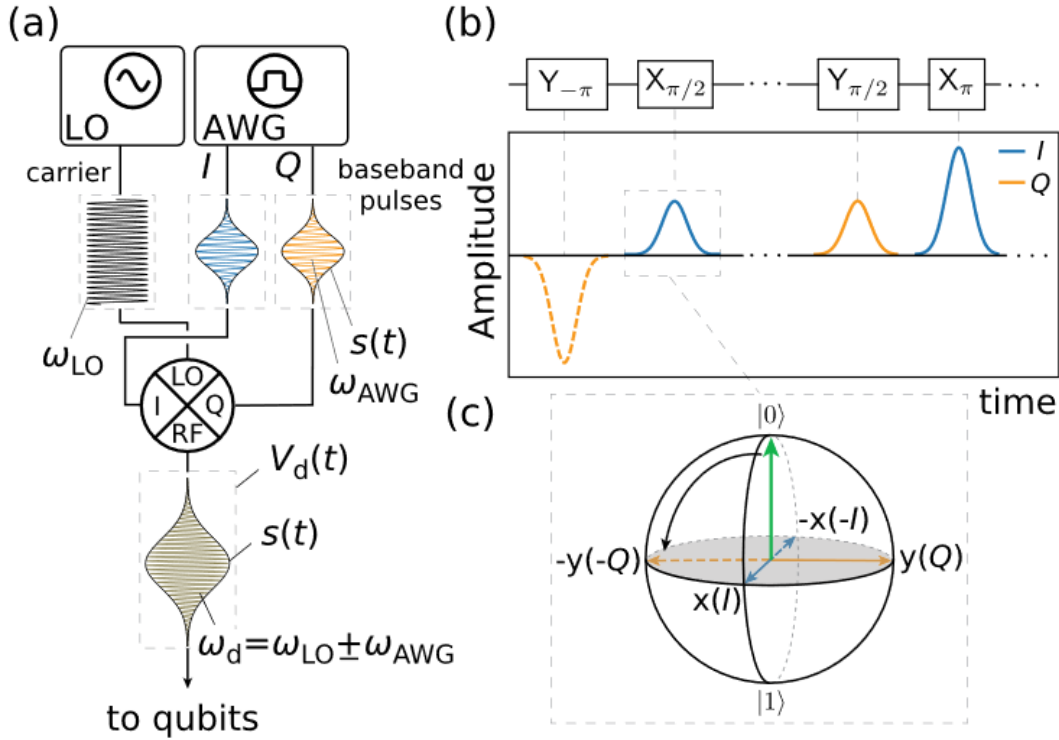


FIGURE 1.5: "(a) Schematic of a typical qubit drive setup. A microwave source supplies a high-frequency signal (ω_{LO}), while an arbitrary waveform generator (AWG) supplies a pulse envelope ($s(t)$), sometimes with a low-frequency component, ω_{AWG} , generated by the AWG. The IQ-mixer combines the two signals to generate a shaped waveform $V_d(t)$ with a frequency $\omega_d = \omega_{LO} \pm \omega_{AWG}$, typically resonant with the qubit. (b) Example of how a gate sequence is translated into a waveform generated by the AWG. Colours indicate the I and Q components. (c) The action of an $X_{\pi/2}$ -pulse on a $|0\rangle$ state to produce the $|-i\rangle = \frac{1}{\sqrt{2}}(|0\rangle - i|1\rangle)$ state." Taken from Krantz et al., 2019.

Fig 1.5 outlines the typical in-phase and quadrature (IQ) modulation setup used to generate the pulses. Sub-figure (a) shows how a pulse at frequency ω_d is generated using a low phase-noise microwave generator [denoted the "local oscillator" (LO)], while the pulse is shaped by combining the LO signal

in an IQ mixer with pulses generated in an AWG. To allow for frequency multiplexing, the AWG signal will typically be generated with a low-frequency component, ω_{AWG} and the LO signal will be offset so that $\omega_{LO} + \omega_{AWG} = \omega_d$. We can address multiple qubits (or readout resonators) simultaneously by mixing in more than one frequency $\omega_{AWG1}, \omega_{AWG2}, \dots$, via the superposition of individual drives.

The I (Q) input of the IQ mixer will multiply the baseband signal to the in-phase (out-of-phase) component of the LO. In sub-figure (b) the comparison between XY gates in a quantum circuit and the corresponding waveforms generated in the AWG are shown. The inset shows an example of a gate.

1.4.2 Virtual Z gate

The distinction between x - and y -rotations is merely a choice of phase on the microwave signals, and the angle to be rotated is given by $\Theta(t)$, both of which are generated using an AWG. Since the choice of phase ϕ has an arbitrary starting point, changing the phase effectively changes rotations around x to rotations around y . This is akin to applying a Z_π rotation to x - and y -rotations, where $Z_\pi X_\pi = iY_\pi$ and $Z_\pi Y_\pi = -iX_\pi$. This analogy between shifting a phase of an AWG-generated signal and applying Z rotations can be utilized to implement "virtual" Z gates. Such virtual Z gates are "perfect", in the sense that no additional pulses are required, and the gate takes "zero time", and thus the gate fidelity is nominally unity.

1.4.3 The DRAG scheme

When we wrote the Hamiltonian for weak capacitive coupling for X and Y control, we assumed we could ignore the higher levels of the qubit. However, for weakly anharmonic qubits, such as the transmon, this is not a justified assumption since $\omega_q^{1 \rightarrow 2}$ only differs from $\omega_q (\equiv \omega_q^{0 \rightarrow 1})$ by the anharmonicity, $\alpha = \omega_q^{1 \rightarrow 2} - \omega_q$, which is negative and typically around 200 to 300 MHz.

This is sketched in Fig 1.7 where Gaussian pulses with standard deviations $\sigma = \{1, 2, 5\}$ ns have spectral content that leads to nonzero overlaps with $\omega_q^{1 \rightarrow 2} = \omega_q - |\alpha|$ frequency. This leads to two deleterious effects:

1. *leakage errors* which take the qubit out of the computational subspace. This can occur because a qubit in the state $|1\rangle$ may be excited to $|2\rangle$ as a π pulse is applied, or be excited directly from the $|0\rangle$ state since the qubit spends some amount of time in the $|1\rangle$ state during the π pulse.
2. *phase errors* because the presence of the drive results in a repulsion between the $|1\rangle$ and $|2\rangle$ levels, in turn changing $\omega_q^{0 \rightarrow 1}$ as the pulse is applied.

The DRAG procedure (Derivative Reduction by Adiabatic Gate) seeks to combat these two effects by applying an extra signal in the out-of-phase component. The trick is to modify the waveform envelope $s(t)$ according to

$$s(t) \rightarrow s'(t) = \begin{cases} s(t) & \text{on } I \\ \lambda \frac{\dot{s}(t)}{\alpha} & \text{on } Q, \end{cases}$$

where λ is a dimensionless scaling parameter, and $\lambda = 0$ corresponds to no DRAG pulse and $\dot{s}(t)$ is the time derivative of $s(t)$.

The core idea lies in manipulating the control signal sent in such that there is a spectral hole for the frequency corresponding to the $|1\rangle$ to $|2\rangle$ transition. This ensures that even when sending high-speed high-power pulses, the qubit doesn't interact with any photons that could excite it to the second excited state or cause leakage out of the computational subspace.

If we consider the convention of sending our controls through the in-phase (I) component, the DRAG correction would go in via the quadrature (Q) component. The DRAG pulse is accordingly scaled by a DRAG parameter which is used to tune the spectral hole. As the net area of the DRAG correction is zero, see Fig 1.6, there is no effective impact on the final operation, but the spectral hole ensures that during the execution of the operation, no leakage is possible.

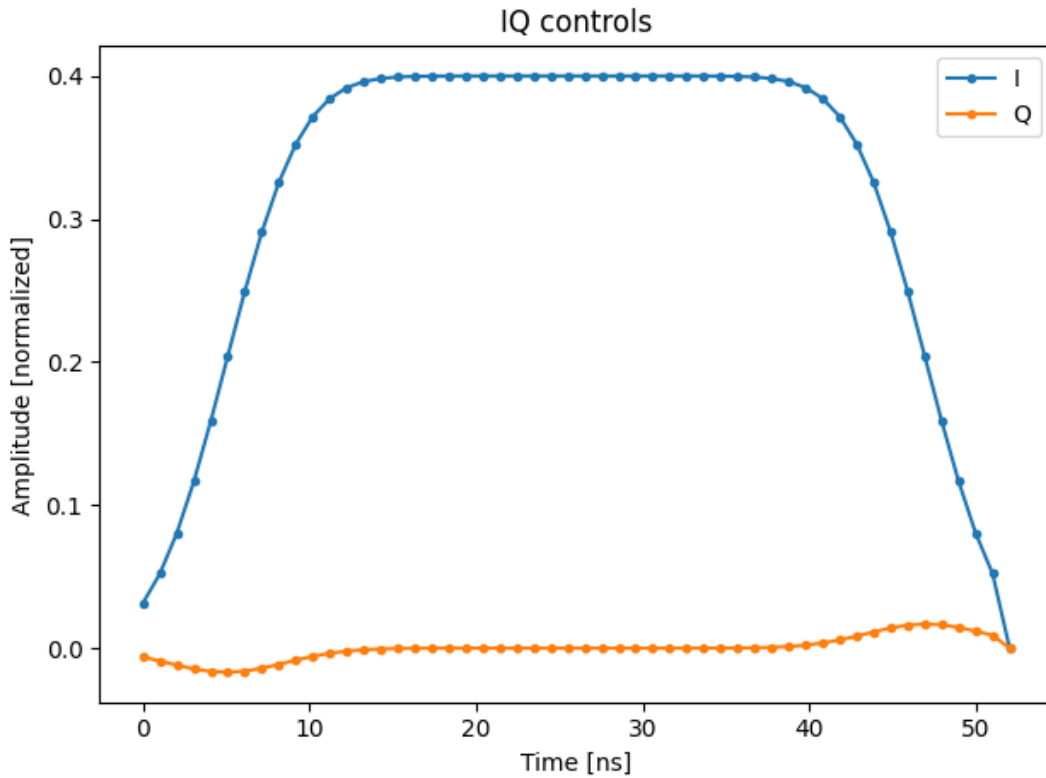


FIGURE 1.6: DRAG modulation for a Gaussian flat top pulse envelope.

The theoretically optimal choice for reducing dephasing error is $\lambda = 0.5$ and an optimal choice for reducing leakage error is $\lambda = 1$. In practice, there

can be a deviation from these two optimal values, often due to pulse distortion in the lines leading to the qubits. An experimental closed-loop calibration experiment for finding the optimal DRAG parameter is discussed later in this thesis.

1.5 Qubit Readout

The ability to perform fast and reliable (high fidelity) readout of the qubit states is an important cornerstone of any quantum processor. Here, we give a brief introduction to how readout is performed on superconducting qubits. The most common readout technique used today in the circuit QED architecture is "dispersive readout" in which each qubit is coupled to a readout resonator. In the dispersive regime, i.e., when the qubit is detuned from the resonator frequency, the qubit induces a state-dependent frequency shift of the resonator from which the qubit state can be inferred by interrogating the resonator.

1.5.1 Dispersive readout

A quantum measurement can be described as an entanglement of the qubit degree of freedom with a "pointer variable" of a measurement probe with a quantum Hamiltonian, followed by a classical measurement of the probe. In circuit QED, the qubit is entangled with an observable of a superconducting resonator, see Fig 1.8, allowing us to gain information about the qubit state by interrogating the resonator - rather than directly interacting with the qubit. A dispersive readout allows us to map the quantum degree of freedom of the qubit onto the classical response of the linear resonator. Thus, optimization of the readout performance is translated to maximising the SNR of the microwave probe tone sent to the resonator, while minimizing the unwanted "back-action" on the qubit.

1.5.2 Measuring resonator amplitude and phase

Let us focus our attention on how to probe the resonator to "read out the qubit", i.e., best distinguish the two classical resonator signatures corresponding to our qubit states, see Fig 1.8. The best state discrimination is obtained by maximizing the separation between the two states in the (I, Q) -plane, i.e., the in-phase and the quadrature component of the voltage. Once we have picked the resonator probe frequency, the quantum dynamics of the qubit can be mapped onto the phase of the classical microwave response, which can be measured using heterodyne detection.

A readout event starts with a short microwave tone directed to the resonator at the resonator probe frequency ω_{RO} , after interacting with the resonator, the reflected (or transmitted) microwave signal has the form

$$s(t) = A_{RO} \cos(\omega_{RO}t + \theta_{RO}),$$

where ω_{RO} is the "carrier frequency" used to probe the resonator. A_{RO} and θ_{RO} are, respectively, the qubit-state-dependent amplitude and phase that we want to measure.

A direct means to extract I and Q is to perform "heterodyne" measurement using an analog "I-Q mixer". The readout signal $s(t)$ and a reference local-oscillator signal are fed into the mixer via the RF and LO mixer ports, $y(t) = A_{LO} \cos \omega_{LO}t$. The mixer then equally splits the signal and local oscillator into two branches and multiplies them in the following way:

- in the I -branch, the signal $s_I(t) = s(t)/2$ is multiplied by the local oscillator $y_I(t) = (A_{LO}/2) \cos \omega_{LO}t$; and
- in the Q -branch, the signal $s_Q(t) = s(t)/2$ is multiplied by a $\pi/2$ -phase-shifted version of the local oscillator, $y_Q(t) = -(A_{LO}/2) \sin \omega_{LO}t$.

The "-" sign arises from the choice of using $A(\cos \omega t + \phi)$ as the reconstructed real signal. At the I and Q ports, the output signals $I(t)$ and $Q(t)$ contain terms at the sum and difference frequencies, generally referred to as an "intermediate frequency," $\omega_{IF} = \omega_{RO} \pm \omega_{LO}$.

The resulting signals are low-pass filtered, passing only the terms at the difference frequency, $I_{IF}(t)$ and $Q_{IF}(t)$ which are then digitized. After digital signal processing, one obtains the static in-phase (I) and quadrature (Q) components, from which one calculates the amplitude A_{RO} and the phase θ_{RO} .

In a heterodyne scheme, a local oscillator at frequency ω_{LO} is offset by an intermediate frequency ω_{IF} to target a unique readout frequency ω_{RO} . Up-conversion techniques such as single-sideband modulation with suppressed carrier (SSB-SC) using balanced I-Q mixers are used to create such readout signals.

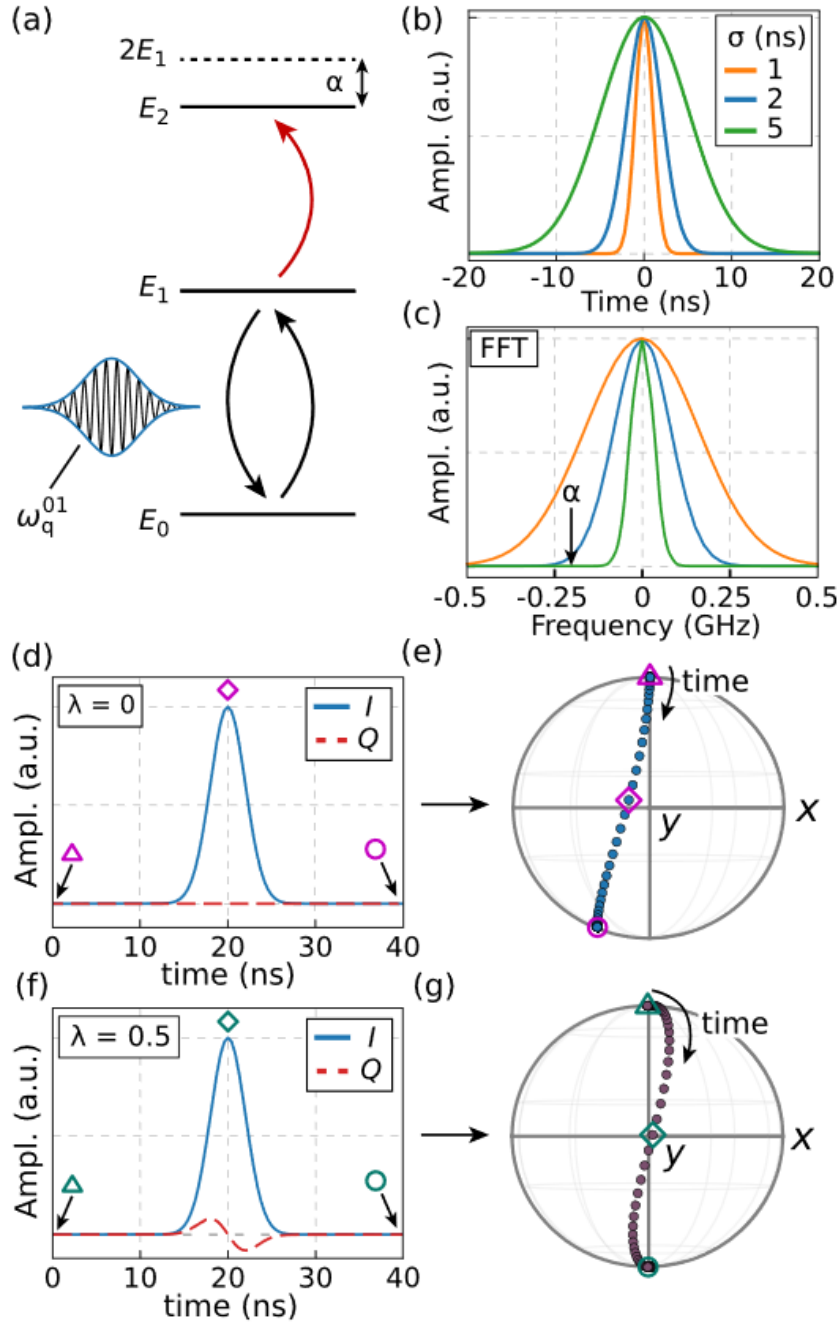


FIGURE 1.7: "(a) Schematic level diagram of a weakly anharmonic transmon qubit subjected to a drive at transition frequency $\omega_d = \omega_q$. (b) Gaussian waveform with standard deviation σ . (c) Fourier transform of (b) shows how the short pulse lengths lead to significant overlap with the $\omega_q^{1 \rightarrow 2}$ transition, separated from ω_q by the anharmonicity α . (d) Waveform of an X_π -pulse without DRAG modulation. (e) Effect of the waveform from (d) on a qubit initialized in the $|0\rangle$ state with $\alpha = -200$ MHz and $\omega_q = 4$ GHz. The dephasing error is visible as a deviation from $|1\rangle$ after the pulse. (f) Waveform of an X_π -pulse with DRAG modulation for a qubit with anharmonicity $\alpha = -200$ MHz and DRAG parameter $\lambda = 0.5$ to cancel dephasing errors (see the text for details). (g) Effect of the waveform from (f) on the same qubit as (e). Calculated using mesolve in the software package QuTiP." Taken from Krantz et al., 2019.

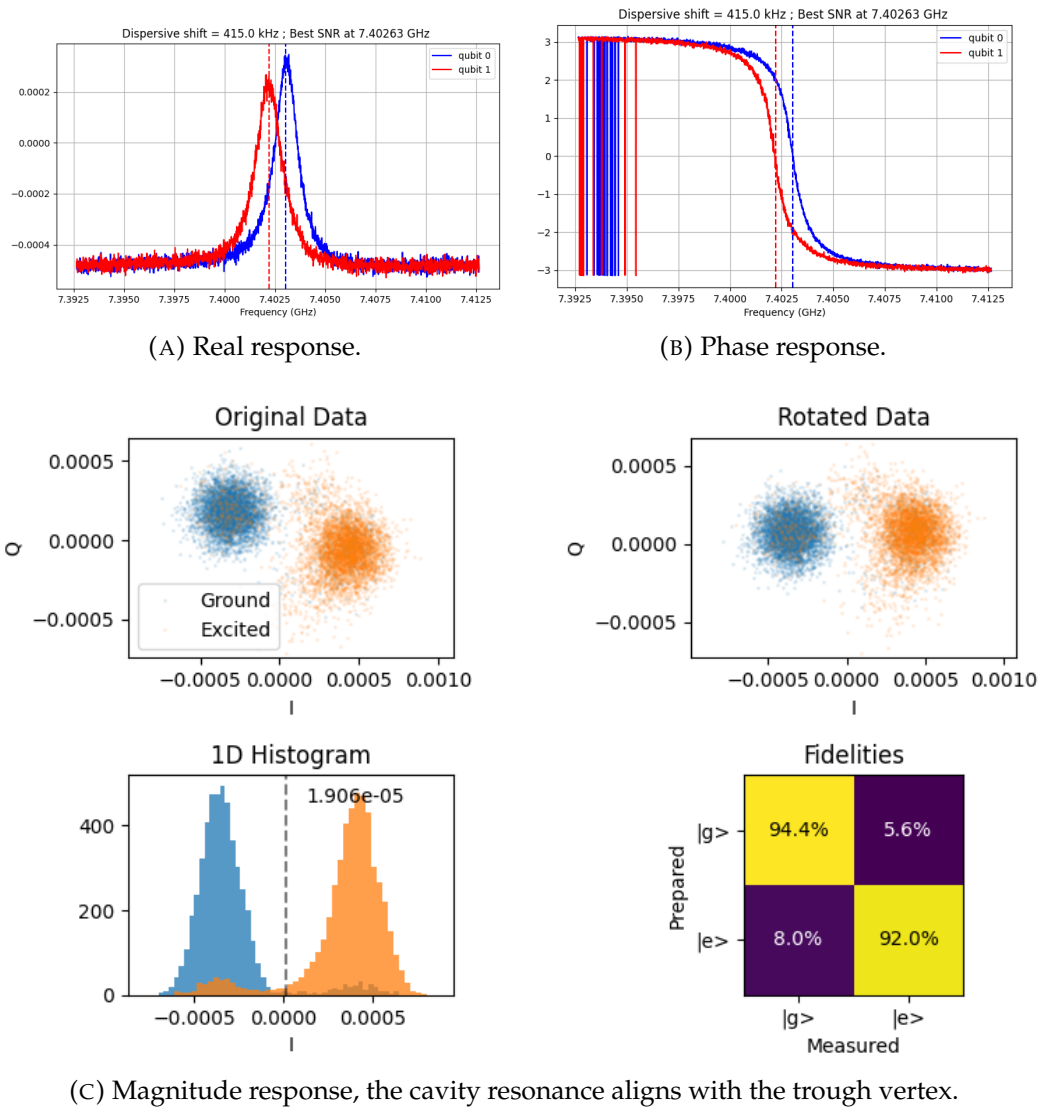


FIGURE 1.8: The dispersive shift used in qubit readout with the real and imaginary profile as well as the observed IQ blob state discrimination and readout fidelity.

2 Tuning up a Superconducting Qubit

In this chapter, we review the series of experiments conducted to tune up a superconducting fixed-frequency transmon once the cool-down of the dilution fridge is completed. This suite of experiments has been developed over many years at the QuMaC lab, some data and plots for expository purposes have been taken from QuMaC data repositories with permission. All experiments after mixer calibration are conducted on the Quantum Machines OPX controller using the Quantum Universal Assembly (QUA) language.

2.1 Mixer Calibration

The program is designed to play a continuous single tone to calibrate an IQ mixer. To do this, the mixer's output is connected to a spectrum analyzer which can be accessed using the VISA interface in the PyVISA Python package. First, the DC mixer offsets are calibrated to ensure the final current leakage is less than -95 dBm. Then, the IQ imbalance amplitude and phase are optimized to ensure minimum current leakage in the mixer sideband. This mixer calibration is done for each qubit and readout resonator independently.

2.2 Time of Flight Calibration

In the Time of Flight experiment, a readout pulse is sent and the raw ADC traces are captured. The data undergoes post-processing to calibrate the time of flight and ADC offsets. Time of flight (TOF) represents the internal processing time and the propagation delay of the readout pulse. This value is utilized to offset the acquisition window relative to when the readout pulse is dispatched. Due to minor impedance mismatches, the signals captured by the OPX might exhibit slight offsets, see Fig 2.1.

2.3 Readout Resonator Spectroscopy

With our mixers calibrated, we now identify the resonant frequency of our readout resonator and update the readout intermediate frequency accordingly. This sequence involves measuring the resonator by sending a readout pulse and demodulating the signals to extract the ' I ' and ' Q ' quadratures across varying readout intermediate frequencies.

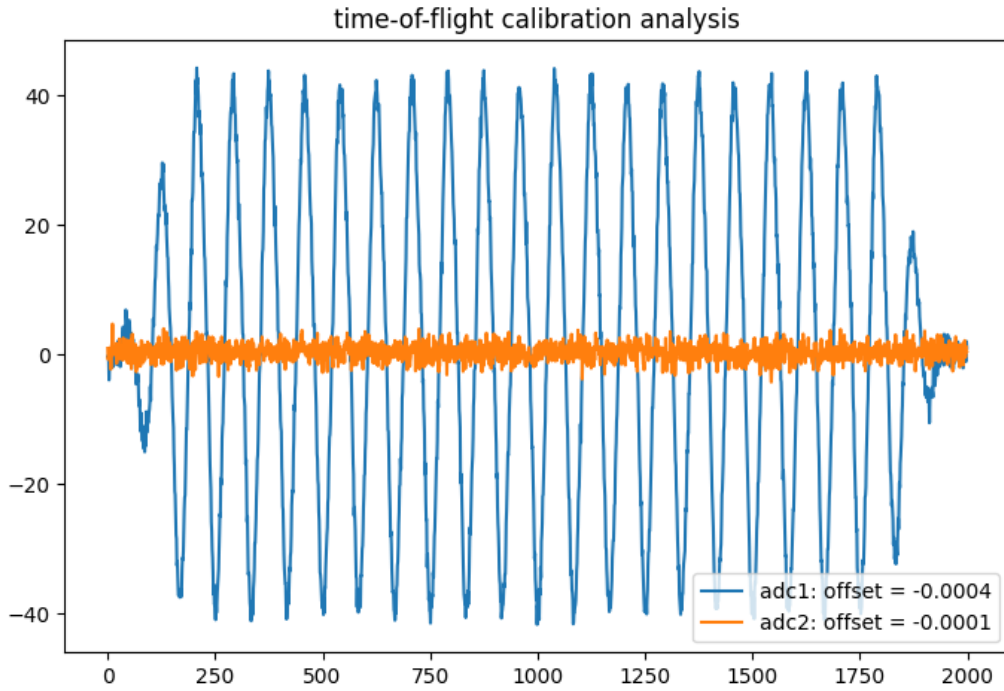


FIGURE 2.1: Time of Flight calibration of ADC offsets.

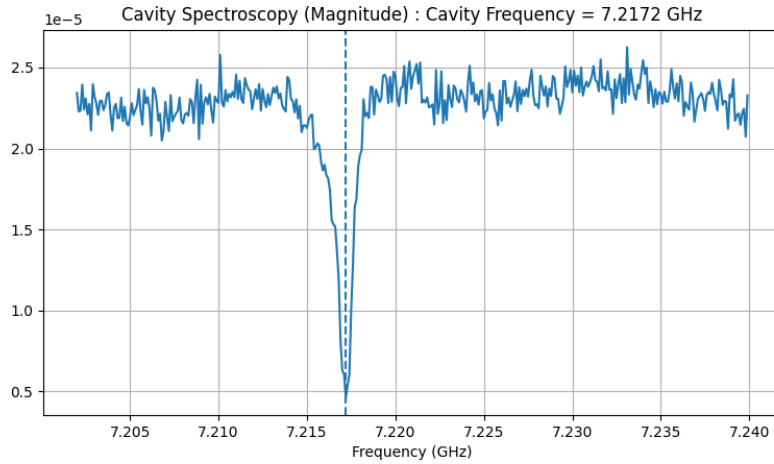
The data is then post-processed to determine the resonator resonance frequency as shown in Fig 2.2. An ideal cavity with no internal loss would result in the phase of the reflection carrying all the information, however, for practical cavities the cavity resonance can be found by noting the trough in the magnitude response or crest in the real response.

2.4 Qubit Spectroscopy

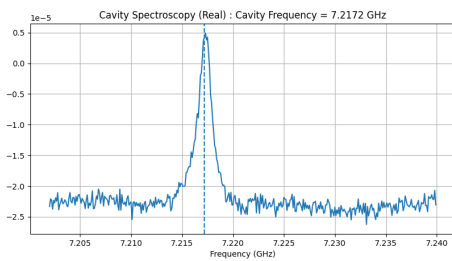
Every qubit has a unique characteristic resonance frequency. An experimentalist usually has a rough idea of the frequency band that the qubit should be located at. Most qubits we work with are in the 5 GHz range, so we calibrate our local oscillator (LO) at 4.8 GHz and sweep over an intermediate frequency (IF) band of ± 350 MHz. On occasion, we may see spurious two-level systems or uncharacterized higher-order transitions due to imperfect thermalization which can result in higher energy levels being occupied.

A key identifier of a qubit is the two-photon excitation from ground to the second excited state. This corresponds to a special resonance peak, at a distance of half anharmonicity from the qubit resonance peak. This is called the $\frac{0-2}{2}$ line. It is usually only visible at high power, as two-photon transitions are rare, and shows up as a very narrow sharp peak, as shown in Fig 2.3.

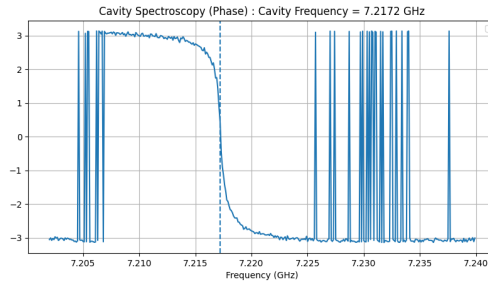
We usually aim for an anharmonicity of -300 MHz, so the $\frac{0-2}{2}$ line is visible at roughly -150 MHz from the qubit peak. If we do not see a line



(A) Magnitude response, the cavity resonance aligns with the trough vertex.



(B) Real response.



(C) Phase response.

FIGURE 2.2: Cavity Spectroscopy of the Readout Resonator

corresponding to this description at the first spectroscopy run, we can tune the power higher until it is visible. As the power increases, we have another identifier of our qubit - the qubit peak will broaden with more power.

Note however that sending more power also results in many more arbitrary, and often spurious, transitions being excited, see Fig 2.4. It is down to the experimentalist's intuition (or a clever algorithm discussed later) to choose the right parameters for power and frequency sweep.

Once the qubit is identified, the power is iteratively reduced with each scan and we narrow our sweep so that we can accurately characterize our qubit frequency, such as Fig 2.5. As power reduces and the qubit peak sharpens with each iteration, we repeat this step until we have a width of about 50 MHz. Going further is unnecessary as our control setup will have some intrinsic bandwidth while sending a signal anyway. Qubit spectroscopy is often the most laborious and time-consuming process in a qubit tune-up.

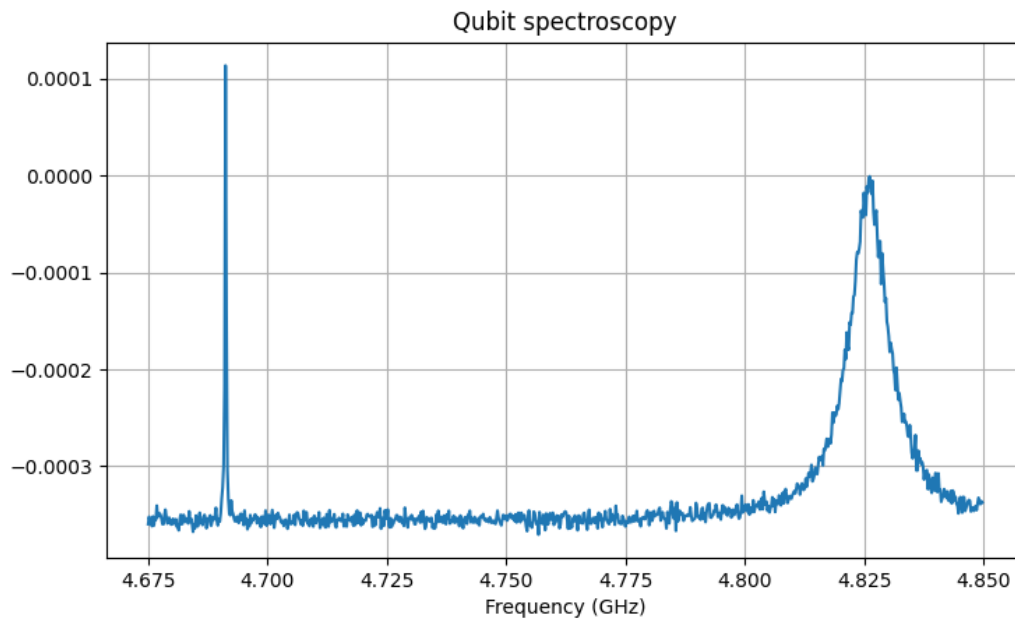


FIGURE 2.3: An ideal qubit spectroscopy scan.

2.5 Time Domain Rabi

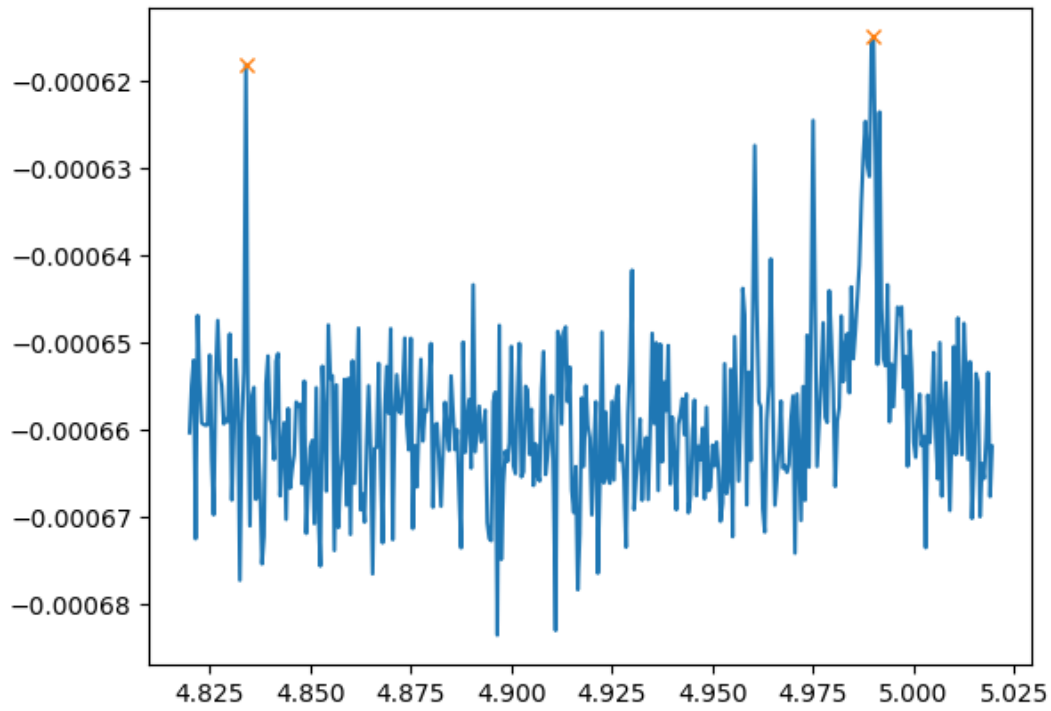
Equipped with the resonant frequency of our qubit, we now send in microwave pulses at a fixed amplitude and measure the qubit state at varying times. This allows us to track the qubit dynamics as a function of time, and after ensemble averaging we see the characteristic Rabi oscillations in both the in-phase (I) and quadrature (Q) components of the complex readout resonator response, see Fig 2.6.

We can adjust the input phase such that all the control signal is sent only in the I component, by adding a phase offset to negate the argument of the complex readout response. This is called IQ calibration and allows us to keep track of only one component which has all the information.

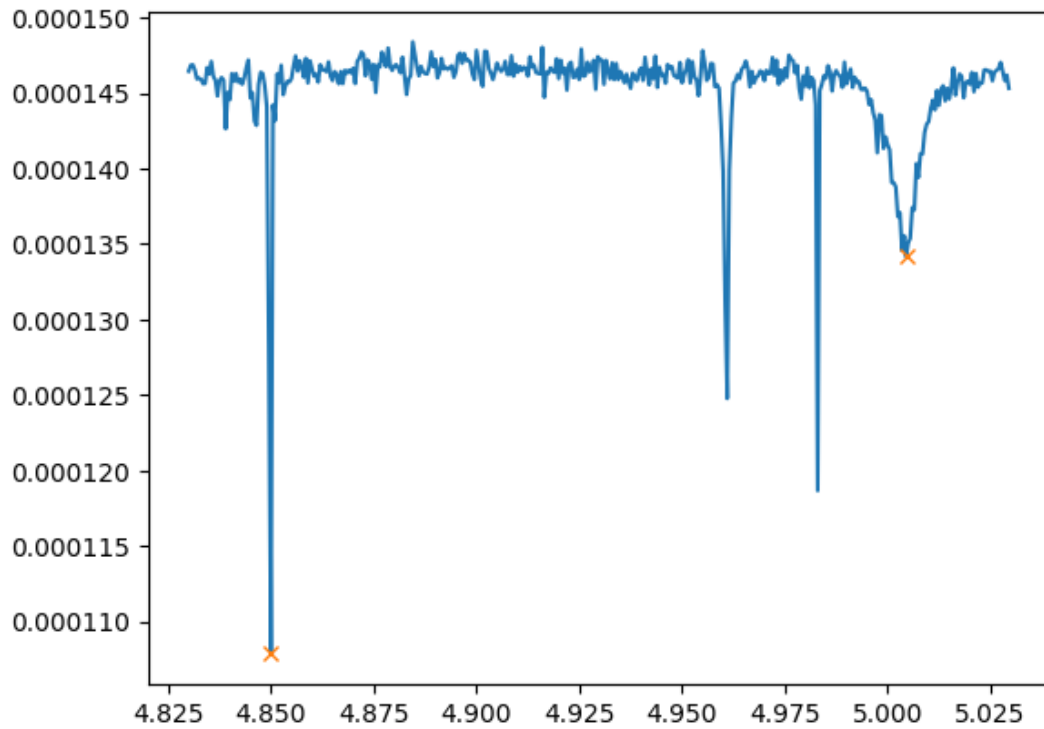
2.6 IQ Calibration

The phase calibration to ensure the signal is only in I or Q quadratures is crucial for state discrimination. We can rotate the IQ "blobs" such that all the information needed is along one axis as shown, see Fig 2.7. The overlap between the two blobs (each corresponding to $|0\rangle$ and $|1\rangle$) is an indication of the readout fidelity i.e., how well we can trust that the qubit has collapsed to the detected state upon measurement.

With the initial guess amplitudes for the π pulse derived from the Time Rabi experiment we ensemble average our measurement of the state of the readout resonator, first after thermalization (qubit in the ground state) and then after applying a π pulse (qubit in the excited state).



(A) Bad signal to noise ratio



(B) Good signal-to-noise ratio

FIGURE 2.4: Two examples of a qubit spectroscopy dataset with bad and good SNR. Observe the presence of multiple peaks. The qubit and $\frac{0-2}{2}$ lines are marked.

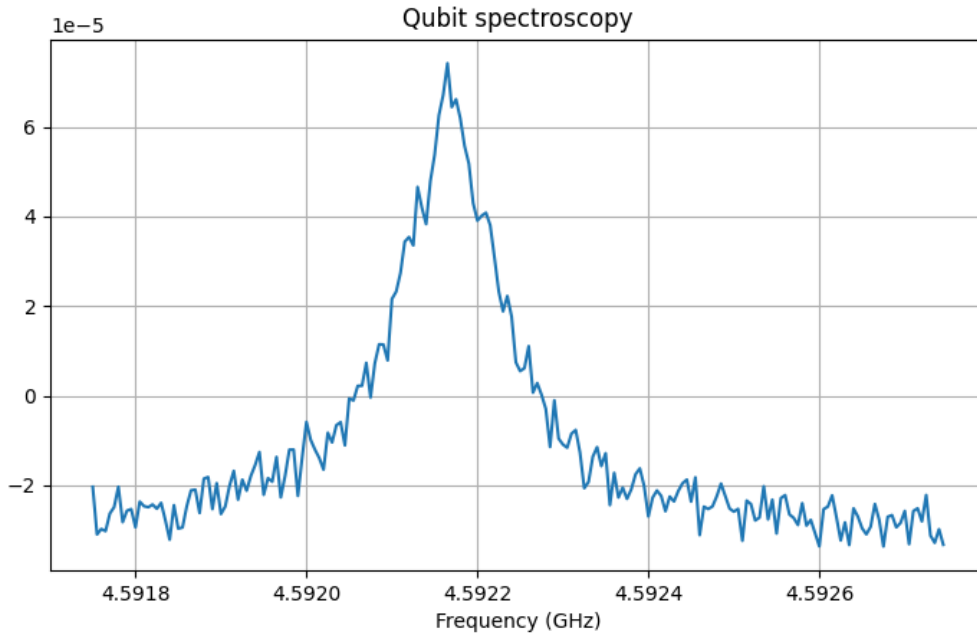


FIGURE 2.5: Well resolved qubit frequency

2.7 Power Rabi Calibration

With our precisely characterized qubit, we now return to fine-tuning our amplitude calibrations for the π and $\frac{\pi}{2}$ pulses. In the Power Rabi experiment, we repeatedly send in the qubit pulse and measure the readout resonator state across different pulse amplitudes and the number of control pulses. This results in increasingly sharper oscillations and amplified inaccuracies in pulse amplitude; now we can successively reduce our amplitude sweep while increasing the number of pulses sent in to determine the optimal amplitude for our pulses up to arbitrary precision. This is shown in Fig 2.8.

In this architecture, Z gates are implemented virtually and are essentially a bookkeeping exercise. We only need to calibrate the X_π and $X_{\frac{\pi}{2}}$ pulses and the corresponding pair for Y pulses can be generated by adding the necessary phase using virtual Z gates. However, in some situations it is possible that some environmental noise sensitivity is asymmetric to the x and y -axes, thus it is always good practice to independently conduct the Power Rabi amplitude calibrations for all 4 pulses - $\{X_\pi, Y_\pi, X_{\pi/2}, Y_{\pi/2}\}$.

After qubit spectroscopy, the Power Rabi experiment is the most time-consuming due to the repeated human input necessary and the need for experimental intuition to choose power and amplitude ranges. An alternative autonomous amplitude calibration routine is detailed later in this thesis.

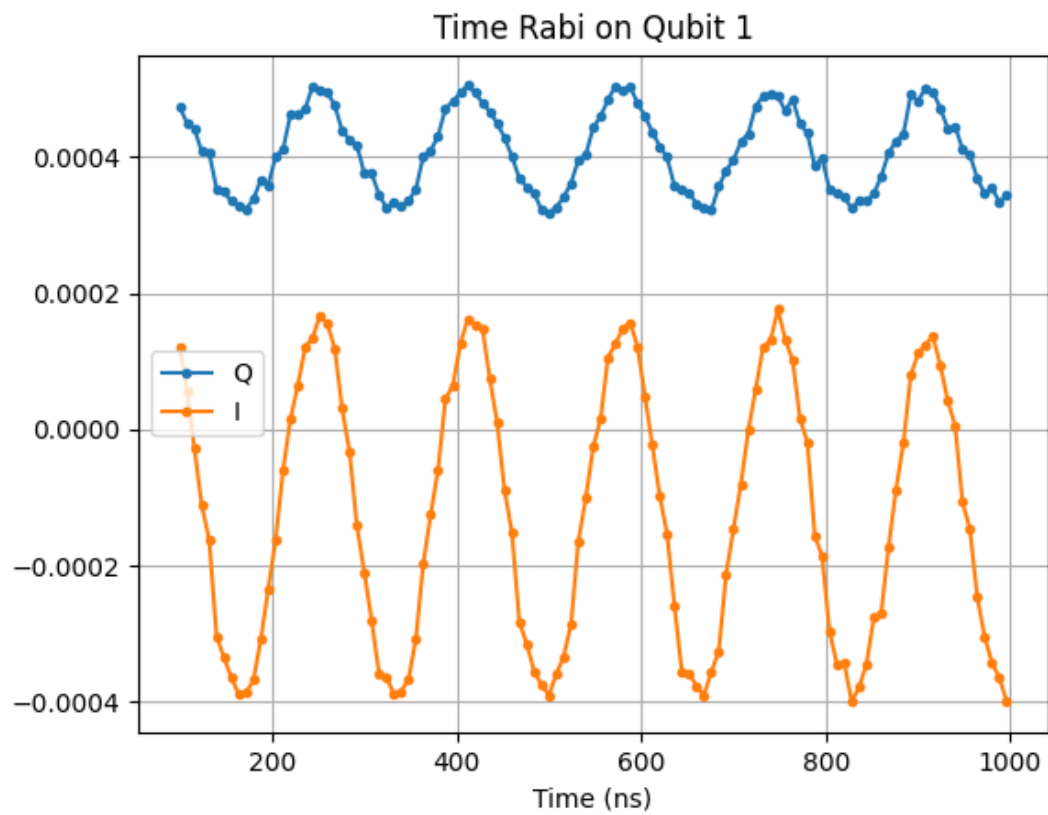
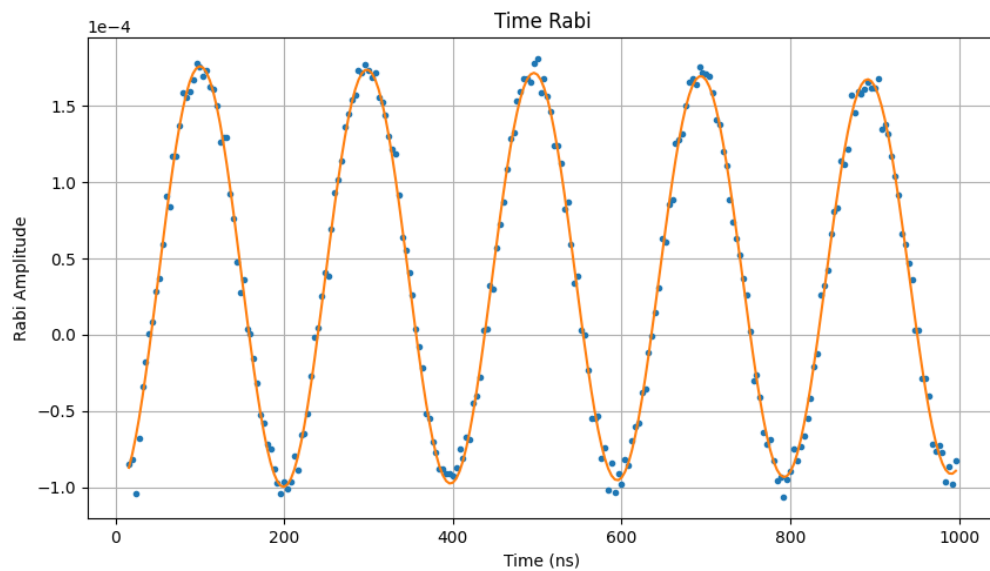
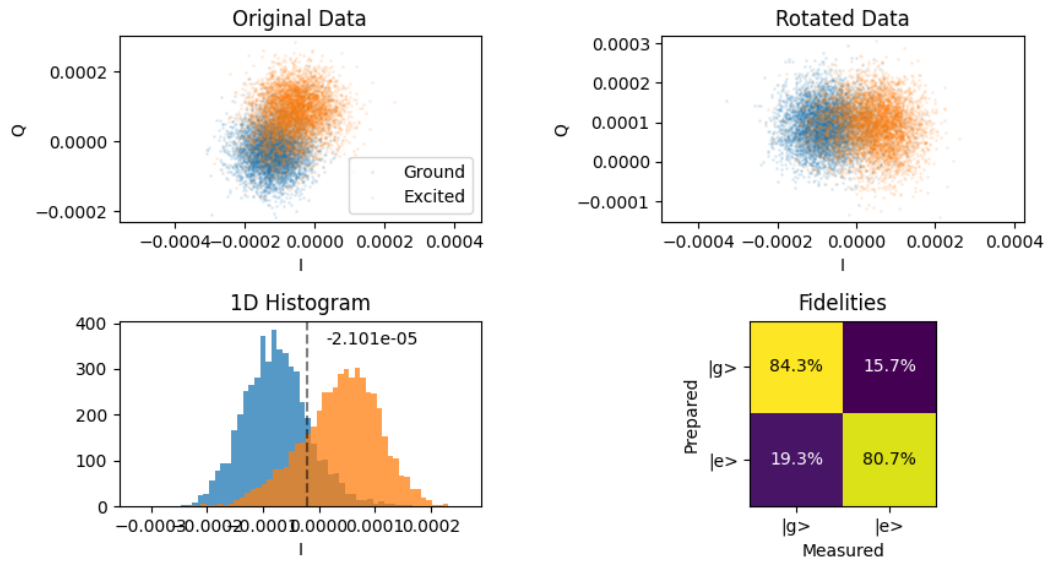
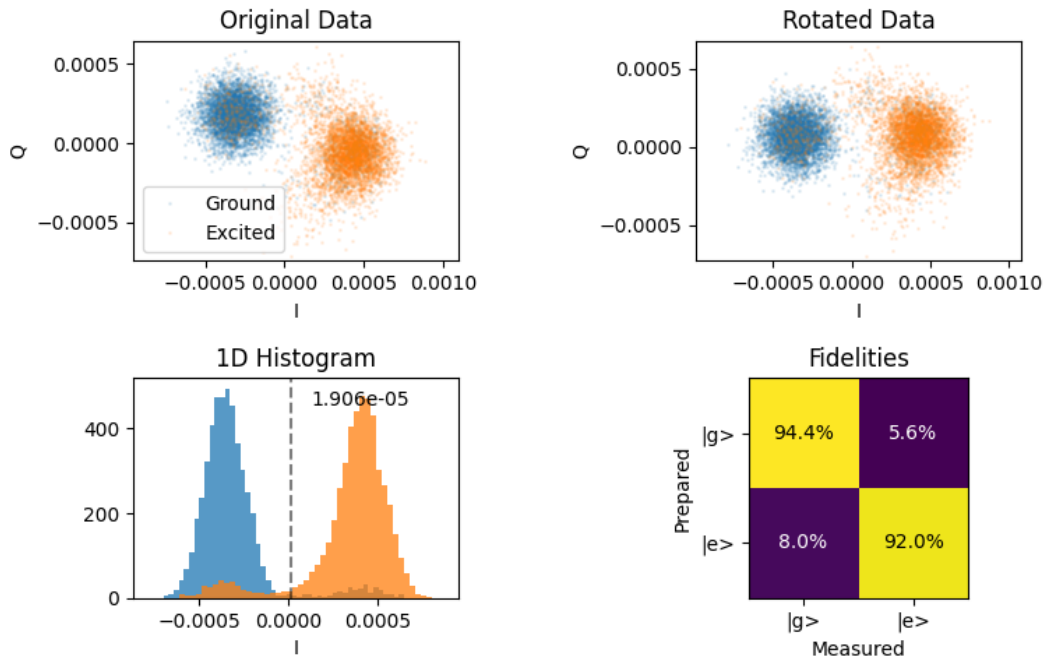
(A) Rabi oscillations in both I and Q quadratures.(B) Fitting the Rabi oscillations in the I quadrature

FIGURE 2.6: Rabi oscillations.



(A) Rotation of overlapping IQ blobs.



(B) Well-separated IQ blobs correspond to high readout fidelity.

FIGURE 2.7: Demonstration of readout fidelity diagnosis using IQ characteristics.

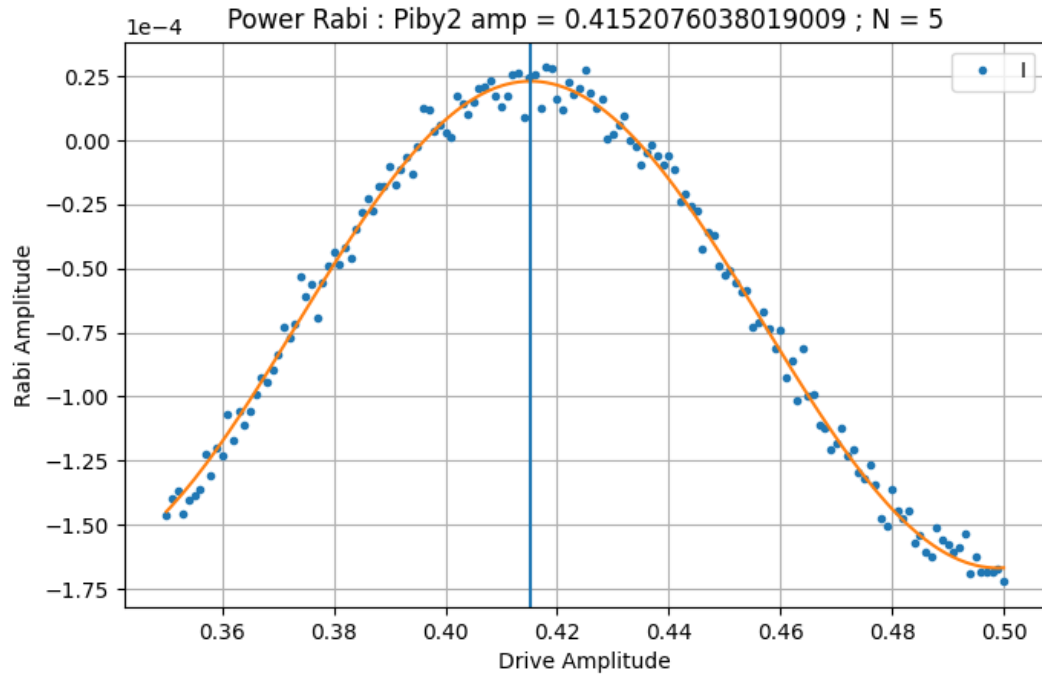
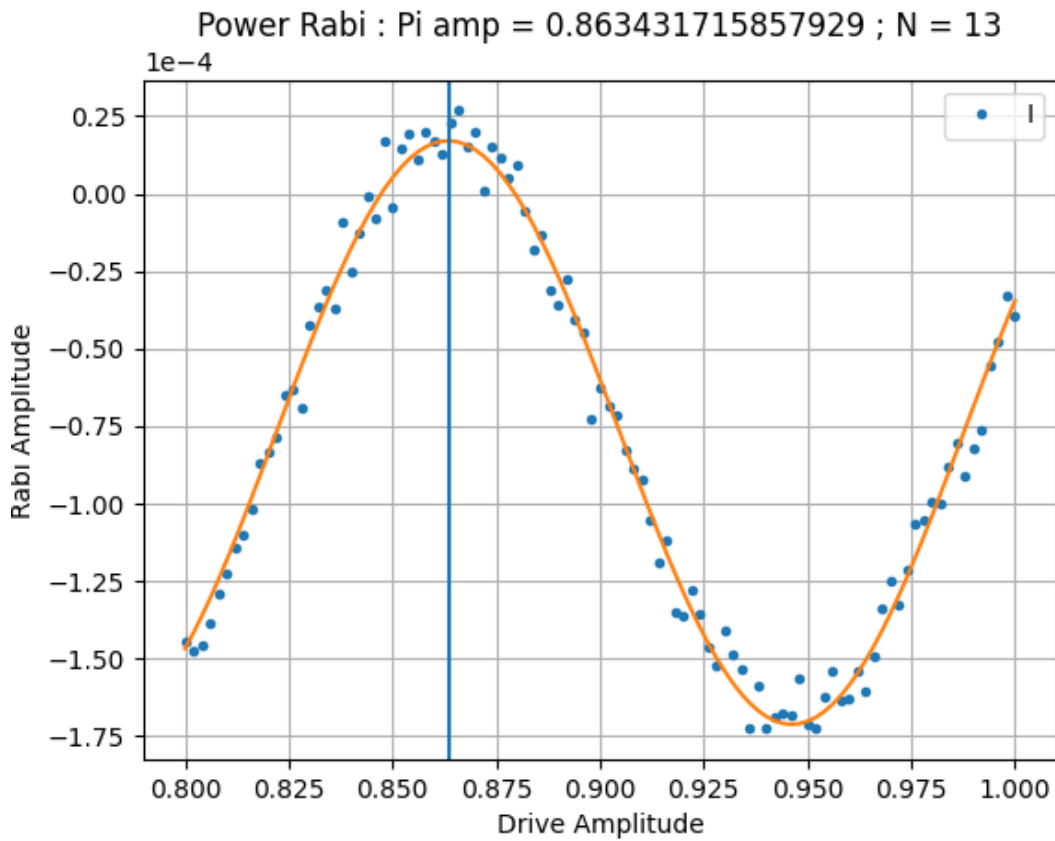
(A) Rough calibration of $\frac{\pi}{2}$ pulse amplitude.(B) Fine calibration of π pulse amplitude. Note that it's close to double of $\frac{\pi}{2}$ amplitude.

FIGURE 2.8: Comparison of the resolution gained by iteratively increasing the number of pulses and narrowing the amplitude range swept.

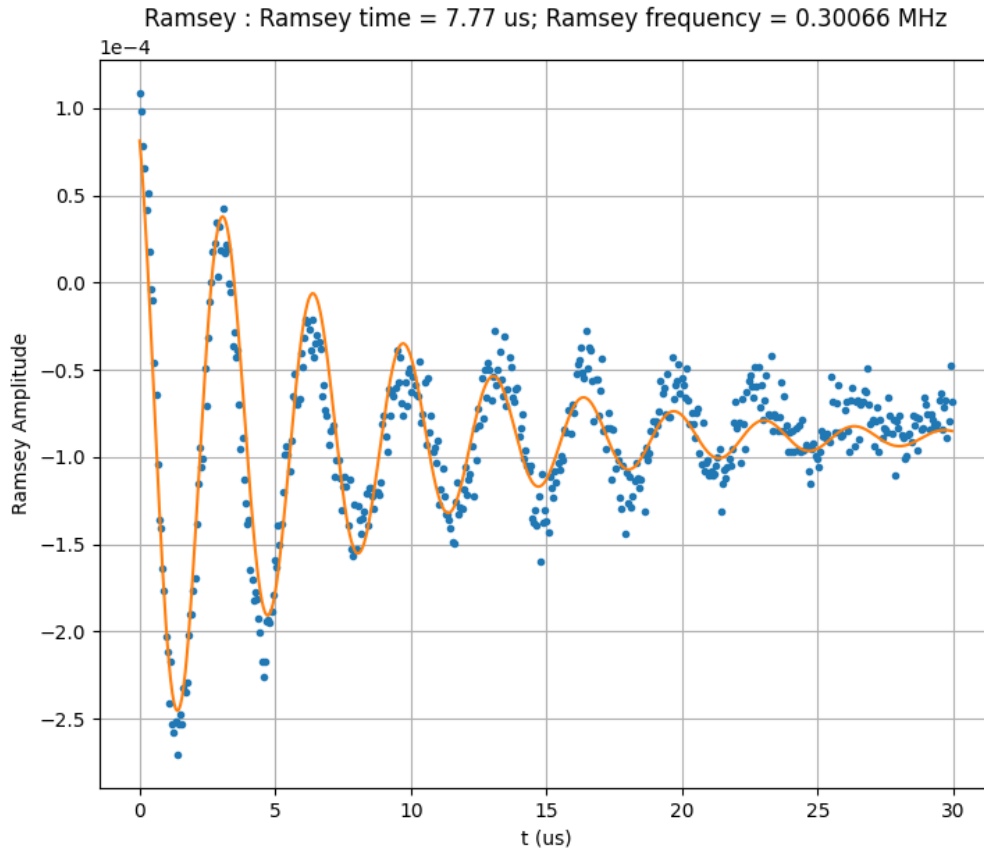


FIGURE 2.9: Ramsey oscillations.

2.8 Time Domain Ramsey

Now with crudely calibrated π and $\frac{\pi}{2}$ pulses and the qubit resonant frequency, we conduct the Ramsey interferometry experiment. This helps us fine-tune our qubit frequency as well as characterize the dephasing noise affecting our qubit.

In this experiment, we send a $\frac{\pi}{2}$ pulse, wait a variable amount of time, send another $\frac{\pi}{2}$ pulse and track the resulting oscillations in the readout response to observe the oscillations. If there is a detuning between the drive and the qubit frequency, the excited state population will oscillate with a gap time at a frequency equal to the detuning, see Fig 2.9. Thus, this can be used to determine the qubit frequency very precisely.

The envelope of the resulting oscillations follows an exponential trend which characterizes the T_2 time of the qubit, also known as Ramsey decay time T_{2R} . The Ramsey decay time is sensitive to fast noise as well as any slow noise affecting the qubit frequency and can be related to the qubit relaxation time by:

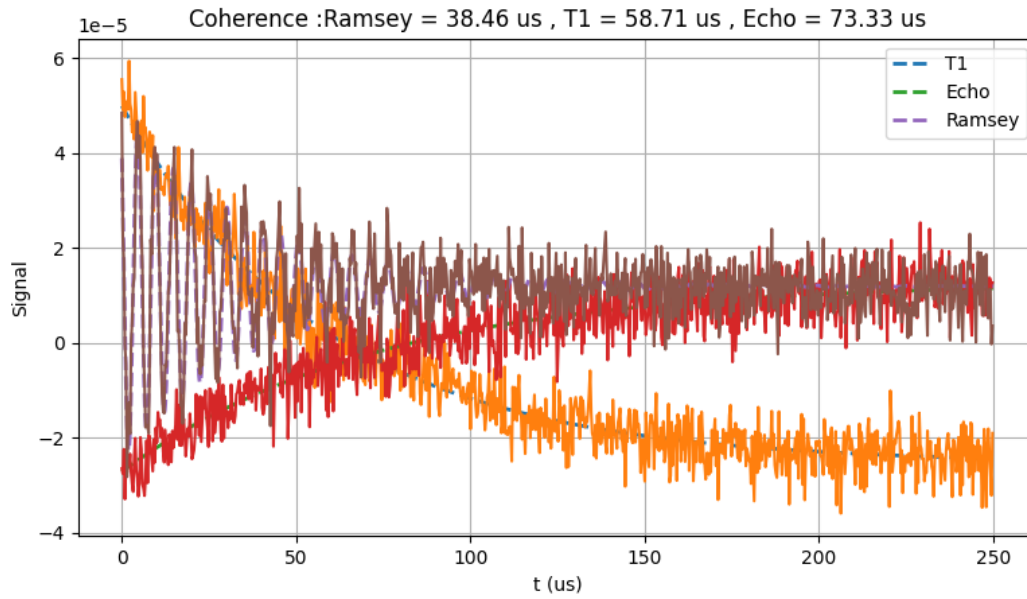


FIGURE 2.10: Coherence experiment for a qubit.

$$\frac{1}{T_{2R}} = \frac{1}{T_\phi} + \frac{1}{2T_1}$$

where T_ϕ is the pure dephasing time of the qubit as defined earlier.

2.9 Interleaved Coherence

The interleaved coherence experiment completely characterizes the various relaxation mechanisms of our qubit using the T_1 measurement, Ramsey interferometry and Hahn echo experiments described earlier in Section 1.3. In the interleaved coherence experiment, each data point for a given time step is taken simultaneously for all 3 experiments, ensuring that they are all equally exposed to any local noise that evolves with time. This addresses the possibility that the noise environment can change if the three experiments were run sequentially. The post-processed results can be seen in Fig 2.10.

2.10 Randomized Benchmarking

For computational purposes, we also benchmark the pulses we have calibrated using Clifford-gate Randomized Benchmarking (RB) experiments. This is one of the most prevalent techniques to quantify the fidelity of qubits. The Clifford group consists of π and $\frac{\pi}{2}$ pulses along X and Y as well as the identity operation. If the 6 vertices of the symmetry axes of the Bloch sphere are considered, the Clifford group of gates allows one to go from any one vertex to another.

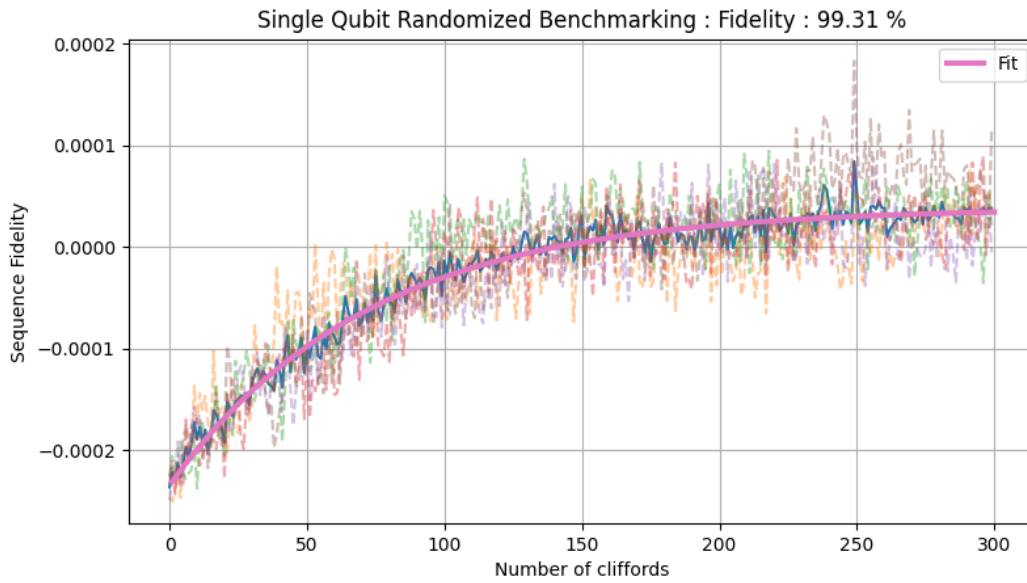


FIGURE 2.11: Single qubit standard RB.

In randomized benchmarking, random sequences of Clifford operations of varying lengths are run on the qubit and ensemble-averaged. Each sequence is suffixed with an inverse gate (that also belongs to the Clifford group) such that the effective unitary operation is an identity operation. As the lengths of the sequences increase, the errors accumulate and we observe larger deviations from the identity operation. This deviation from identity is then quantified as the fidelity of the qubit gate-set. This is also labelled as the error-per-Clifford. The single qubit randomized benchmarking experiment can be seen in Fig 2.11.

Several variants of randomized benchmarking exist that address specific error sources - like leakage out of the computational subspace, which shall be discussed shortly. Another popular modification of RB is Interleaved RB, where the fidelity of a particular gate is tested rather than the entire gate set. Each random sequence of Clifford gates is spliced with the interleaved test gate, and the deviation from the standard RB characterizes the fidelity of the interleaved gate. Further, for characterizing the effects of qubit cross-talk and truly testing QPU operations, Simultaneous RB is used by running the random sequences on two (or more) qubits concurrently.

2.10.1 Simultaneous Randomized Benchmarking

Simultaneous randomized benchmarking allows one to gauge the impact of multi-qubit cross-talk on the fidelity of operations. By running the randomized sequences in parallel on the qubits, any deviations in amplitude or frequency due to multi-qubit coupling that would affect operations are picked up. This is shown for a pair of qubits in Fig 2.12.

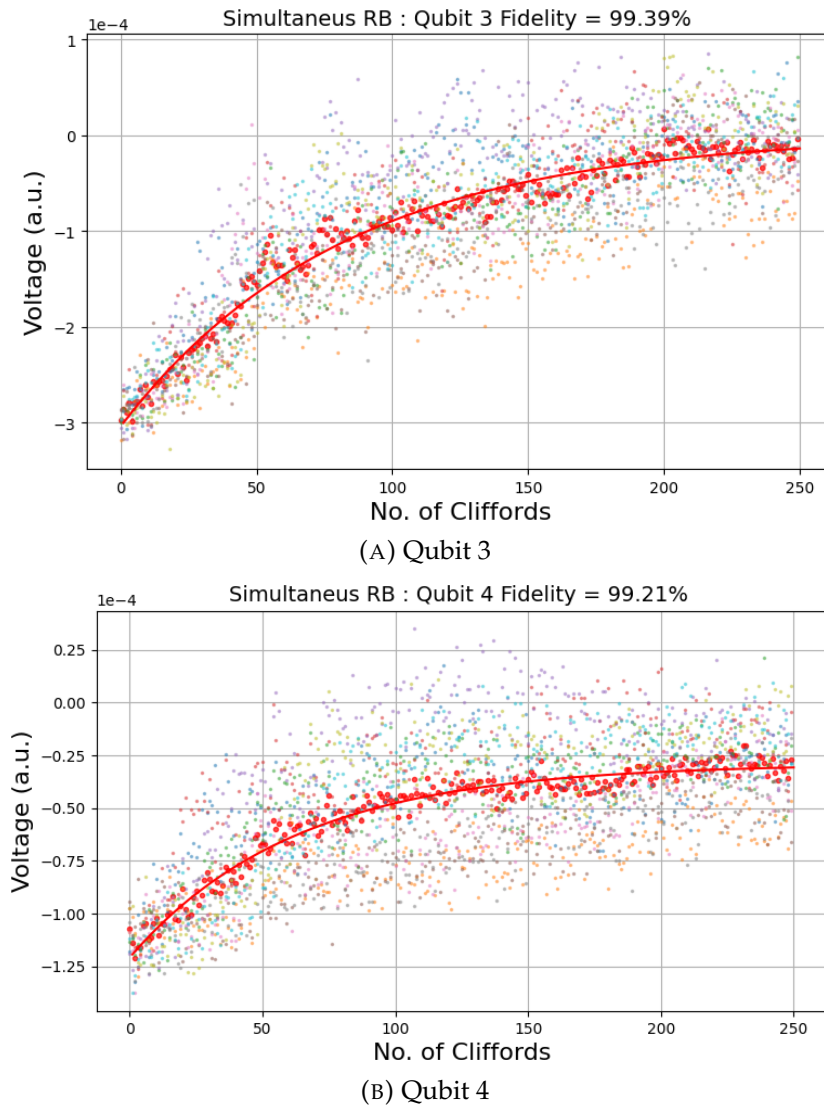


FIGURE 2.12: Simultaneous Randomized Benchmarking on a pair of qubits.

3 Experimental Results

3.1 AutoSpectroscopy

This section introduces the novel AutoSpectroscopy protocol to characterize the transmon qubit. This protocol has successfully characterized real qubits even with significantly noisy signals. The protocol stages are demonstrated in Fig 3.1 and involve the three key functions:

1. *Signal-to-Noise Ratio (SNR)*: The normalized signal received from the demodulated measurement of the readout resonator during qubit spectroscopy is passed through a discrete, linear convolution filter with a window size empirically chosen to capture Lorentzian structures such as resonant peaks. A smaller window size allows higher frequency components to pass through but is also more noise-sensitive. For frequency spans of 500 samples - a sufficient resolution to capture even the very narrow $\frac{0-2}{2}$ transition peak - a window size of 10 has proven sufficient to detect the structure of the narrow $\frac{0-2}{2}$ transition as well.

The filtered signal output from the convolution filter is processed to ensure the length of the filtered signal array and input normalized signal array are the same. The difference between the two arrays is the noise signal array. The power is calculated as the sum of squares of the elements in the array, and the ratio of the filtered signal power to the noise power is defined as the SNR.

2. *Broad Qubit Sweep*: The first scan is conducted at a pulse drive amplitude of 0.5 and from $\omega_{LO} - 350$ MHz to $\omega_{LO} + 350$ MHz. A peak finding function discriminates the normalized signal received on the basis of height and spacing between candidate peaks (which should be half the expected anharmonicity of the qubit). All candidate peaks' full width at half maxima (FWHM) is also recorded. The averaging for each spectroscopy experiment runs until an SNR threshold of 0.5 is breached.

The broadest peak is considered to be the qubit and the narrowest peak is considered to be the $\frac{0-2}{2}$ transition. A global list keeps note of the frequency index of the widest peak (qubit candidate) to a 0.01 resolution. If the anharmonicity calculated from the frequencies of the candidate qubit and $\frac{0-2}{2}$ transition is within 50 MHz of the expected anharmonicity, we conclude our broad qubit sweep. If not, we rerun the experiment with increased power, i.e., pulse drive amplitude.

As the qubit peak will broaden with increasing power, the frequency associated with the candidate with maximum FWHM will be increasingly likely to be the qubit. If the $\frac{0-2}{2}$ condition (anharmonicity) is not satisfied within a few iterations, the mode of the global list tracking the qubit frequency is taken as the correct qubit frequency. This contingency is backed by the fact that the peak which has consistently broadened run-after-run will be the qubit.

3. *Fine Qubit Sweep*: Once, the broad qubit sweep has concluded and the qubit frequency and FWHM are known, the fine qubit sweep narrows the frequency span to $\pm 3 * \omega_{q,FWHM}$ from the qubit frequency, and reduces the power. The averaging for each spectroscopy experiment runs until an SNR threshold of 0.8 is breached, note that this is higher than the broad qubit sweep because here we have already narrowed our scan to the neighbourhood of the qubit and will not encounter spurious two-level systems.

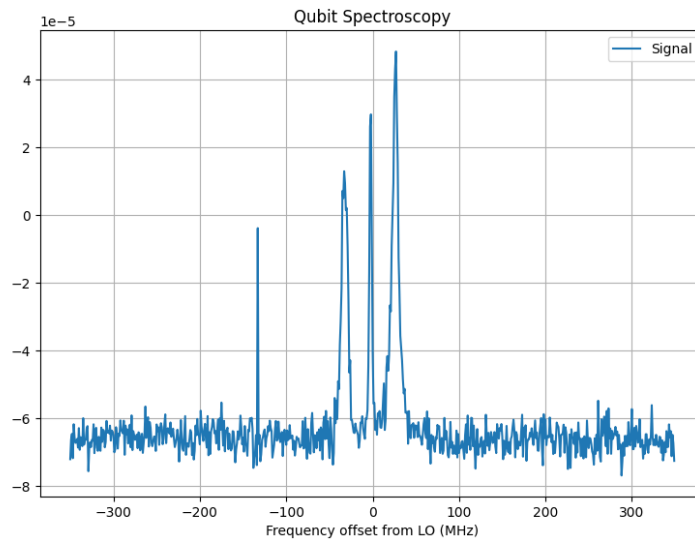
As the power is reduced, the qubit peak sharpens and as we reduce the frequency span we are able to improve the precision of our qubit frequency characterization. This can be extended arbitrarily, we terminate at a FWHM of 50 KHz. In case the fine qubit sweep locks onto a frequency value that deviates from the broad qubit sweep output by more than 0.01, we rerun the fine qubit sweep with lesser power to further sharpen the qubit peak profile.

This protocol has been extensively tested on noisy datasets, various qubit designs, and multiple cooldowns, in the presence and absence of spurious two-level systems and for a range of anharmonicities. It allows the experimentalist to simply feed in the expected anharmonicity of the qubit and requires the following experiments to have been completed before execution:

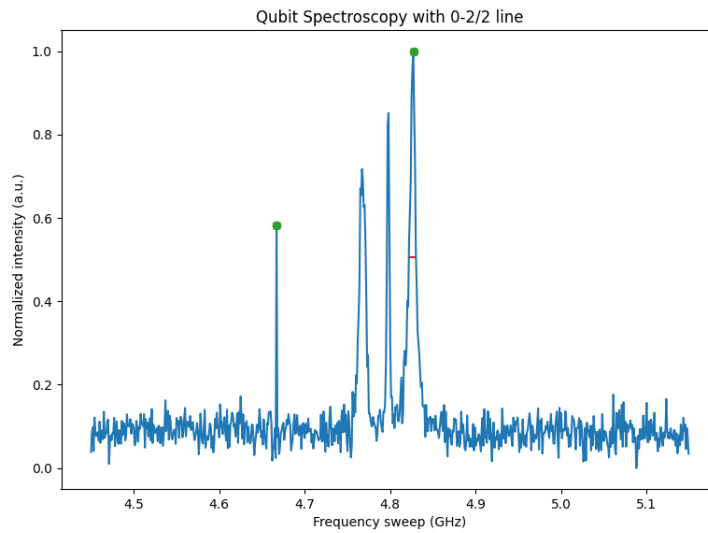
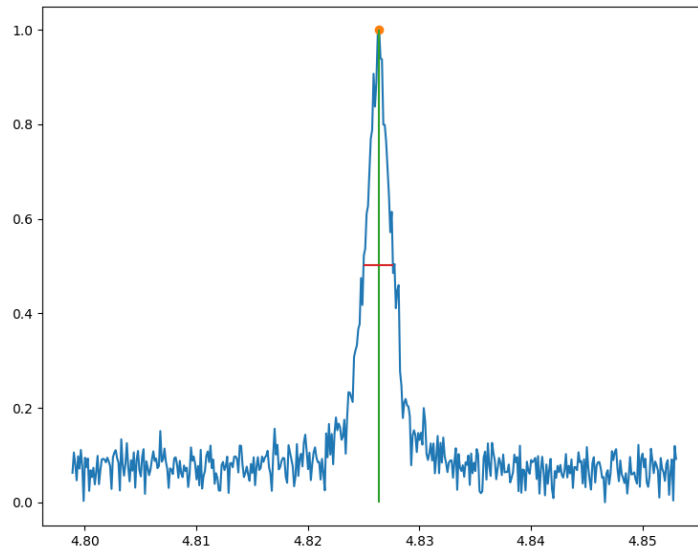
1. Mixer calibrations
2. Time of Flight calibration
3. Readout resonator spectroscopy

3.2 ALLXY Pulse Calibration

In this section, we discuss the implementation of the ALLXY pulse calibration protocol introduced in (Reed, 2013). While Rabi and Ramsey calibrations suffice for most basic single-qubit experiments, better-calibrated rotations are necessary for applications where a high quantitative value of fidelity is the goal, such as for algorithms and state tomography. For this, we need more sophisticated tune-up sequences.



(A) The initial broad sweep.

(B) Identifying the qubit and $\frac{0-2}{2}$ peak.

(C) Successfully narrowed qubit peak to 50KHz FWHM resolution.

FIGURE 3.1: Successive stages of the AutoSpectroscopy code.

While a Rabi oscillation is only second-order sensitive to the Rabi rate at its poles (though more sensitivity can be recovered by curve fitting the oscillation), concatenations of $\frac{\pi}{2}$ and π pulses are, for example, first-order sensitive and errors can be intentionally amplified with additional π pulse repetitions.

Other parameters like the orthogonality of rotations around the X and Y axes, pulse corrections for higher excited transmon states, reflections, and the consequences of simultaneous pulses or coupling to other qubits are also not reliably measured by Rabi and Ramsey experiments.

All combinations of one or two single-qubit rotations around the x and y -axes by an angle of $\frac{\pi}{2}$ and π are performed on a qubit which is then measured. These are a member of the “Clifford set” of quantum gates. Each pulse combination is sensitive to various errors to varying degrees. Each error carries a distinctive signature deviation from the ideal response, which can lead to a simultaneous diagnosis of multiple linearly independent errors, and appropriate corrective measures can be taken. In each case, the qubit should end up on the North pole, equator or South pole of the Bloch sphere.

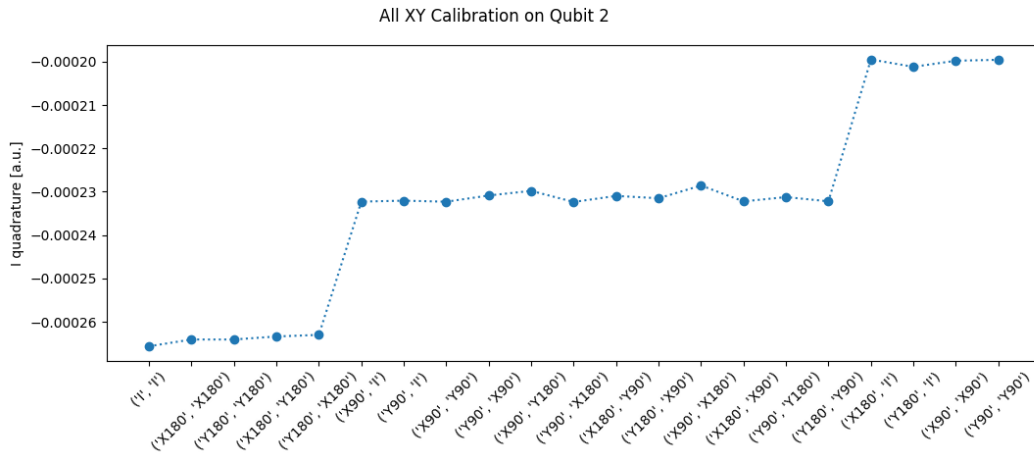
3.2.1 Simultaneous ALLXY

Qubit cross-talk or qubit-qubit coupling can be picked up by ALLXY. The hybridization of coupled qubits leads to an effective ZZ interaction which causes the drive controlling one qubit to be dependent on the state of the other qubit. By definition, single qubit rotations should not depend on the state of other qubits. Composite pulse sequences exist that are designed to be robust to a variety of errors, simultaneous ALL-XY can be used to characterize the type of error the qubits are most susceptible to and help choose an appropriate composite sequence. Further, it allows one to test and validate the choice by a clear visual and intuitive demonstration.

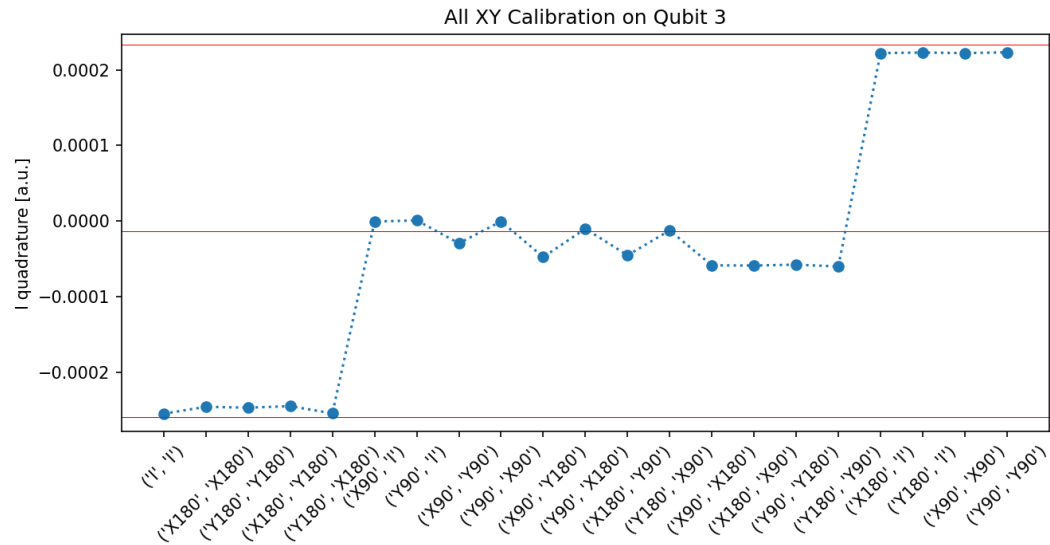
3.2.2 DRAG parameter calibration

The calibration of the DRAG coefficient involves running a sequence consisting of successive $X_\pi Y_{\pi/2}$ and $Y_\pi X_{\pi/2}$ pulses to the qubit while varying the DRAG coefficient. Indeed, this is a special case of the ALLXY pulse calibration. The qubit is reset to the ground state between each sequence and its state is measured and stored. Each sequence will bring the qubit to the same state only when the DRAG coefficient is set to its correct value. The experimentally calibrated value of the DRAG parameter can be found as shown in Fig 3.3.

The DRAG coefficients were calibrated for all 4 single qubit pulses (X_π , Y_π , $X_{\pi/2}$, $Y_{\pi/2}$) and an overnight comparison of fidelity measurements by simultaneous randomized benchmarking for a pair of qubits (Q1, Q4) was carried out, see Fig 3.4. We compared calibrated pulses with and without



(A) The rough structure expected from ALLXY measurement.



(B) With added reference lines for ground, equator and excited states.

FIGURE 3.2: ALLXY pulse sequence on a real qubit.

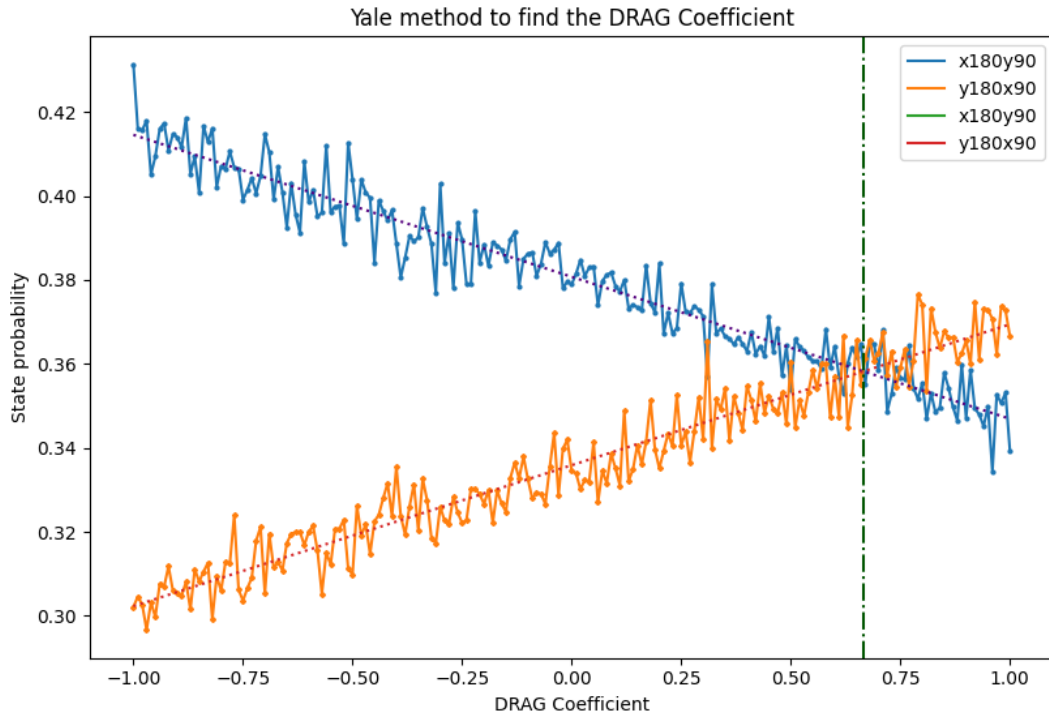


FIGURE 3.3: Closed loop calibration of DRAG parameter

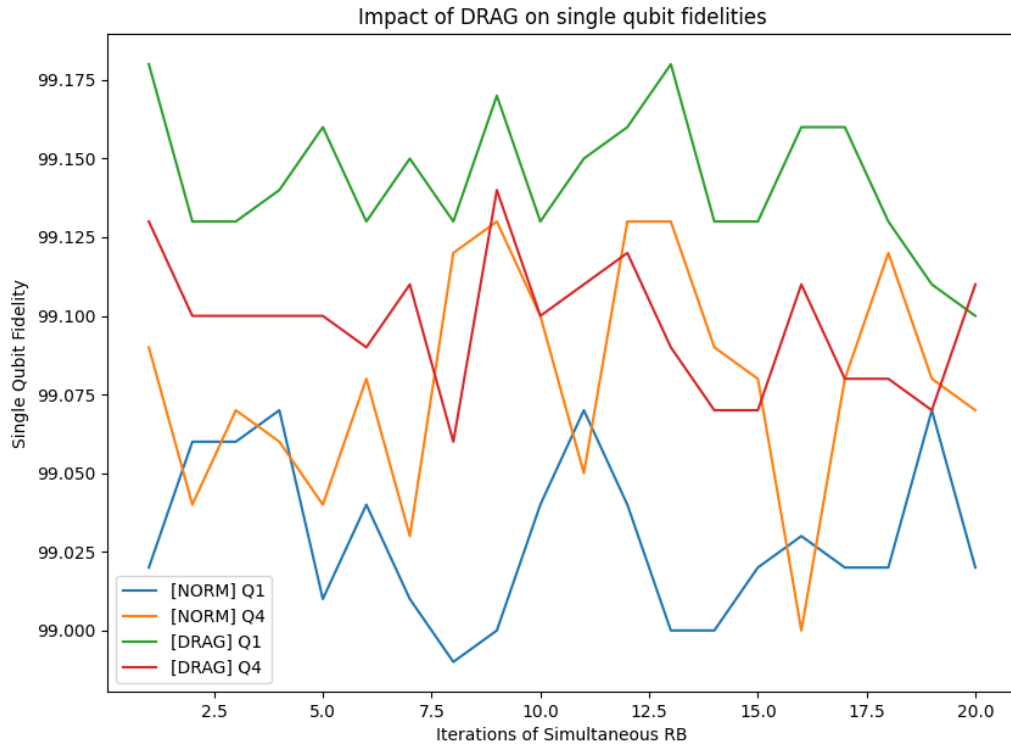
DRAG correction and observed that for Q1 (high SNR) there was a statistically significant improvement in fidelity, while for Q4 (low SNR), on average the DRAG pulse performed at least just as well as the uncorrected pulse.

3.3 Closed-Loop Amplitude Calibration

In this section, we discuss a closed-loop amplitude calibration experiment to replace the resource-intensive Power Rabi calibration. It is based on a variant of Randomized Benchmarking called optimized randomized benchmarking for immediate tuneup (ORBIT) (Kelly et al., 2014), and implemented using a protocol called adaptation by hybrid optimal control (Ad-HOC) (Egger and Wilhelm, 2014). The ORBIT figure of merit is optimized using the Nelder-Mead simplex optimization algorithm (Nelder and Mead, 1965) as it is particularly well suited for bounded constrained minimization and is robust in diverse applications.

3.3.1 Ad-HOC protocol

When quantum systems are improperly characterized, theoretical model-based pulse shapes need to be tuned directly on the experiment. While clever experiments can be designed to calibrate analytical pulse shapes, due to the lack of analytical insight and a large search space this is not feasible for numerical pulses defined by many parameters.



(A) Overnight fidelity comparison of DRAG and normal pulses.



(B) Including 2 orders of standard deviation

FIGURE 3.4: Clear improvement in fidelity using DRAG is observed overnight.

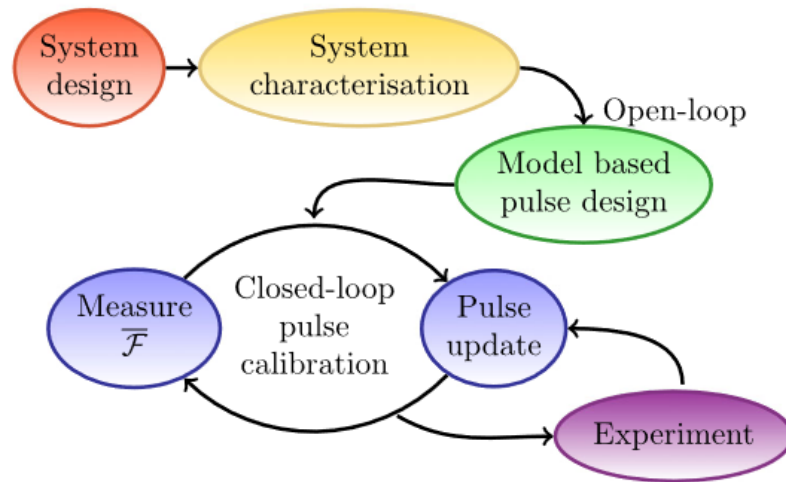


FIGURE 3.5: "Ad-HOC protocol: The physical system and surrounding control and measurement apparatus are designed taking control problems into consideration. For instance, the AWG has to have sufficient bandwidth for the desired control task. The system is then characterized with the best possible precision. Using the resulting parameters the control pulses are created. These are then fine-tuned to the system using closed-loop OCT. The pulses are then ready to be used in the experiment and can be recalibrated at a later time to account for drift."

Taken from Egger and Wilhelm, 2014.

Ad-HOC is a hybrid open/closed-loop optimal control method that is designed to overcome the shortcomings of an assumed physical model, errors in the controls themselves and inaccurate knowledge of the parameters. It uses the physical system itself as feedback to calibrate the control pulses, see Fig 3.5. Ad-HOC can be integrated with ORBIT as introduced later to achieve closed-loop experimental optimization of control pulses for a wide range of open problems.

3.3.2 Nelder-Mead Algorithm

The Nelder–Mead method is a numerical method used to find the minimum or maximum of an objective function in a multidimensional space. It is a direct search method (based on function comparison) and is often applied to nonlinear optimization problems for which derivatives may not be known. The method uses the concept of a simplex, which is a special polytope of $n + 1$ vertices in n dimensions. Examples of simplices include a line segment on a line, a triangle on a plane, a tetrahedron in three-dimensional space and so forth.

3.3.3 ORBIT figure of merit

Quantum information is stored in continuous amplitudes and phases, so extreme precision in quantum control is necessary for high-fidelity operations that could enable fault tolerance. One can use Clifford-based RB as discussed earlier to map gate errors onto control parameters and feed this back to optimize the gates. This method is fast and scales to arbitrary precision thanks to the comprehensive nature of RB. The sensitivity to fractional error here is independent of gate fidelity. This tool can generally be applied to gate optimization and qubit cross-talk.

In standard RB, gates are characterized by measuring the fidelities of sequences with varying lengths. It has been experimentally shown that optimizing the sequence fidelity at a fixed length improves the gate fidelity. This approach - using the sequence fidelity from randomized benchmarking as a fitness metric for gate performance - optimized randomized benchmarking for immediate tune-up (ORBIT).

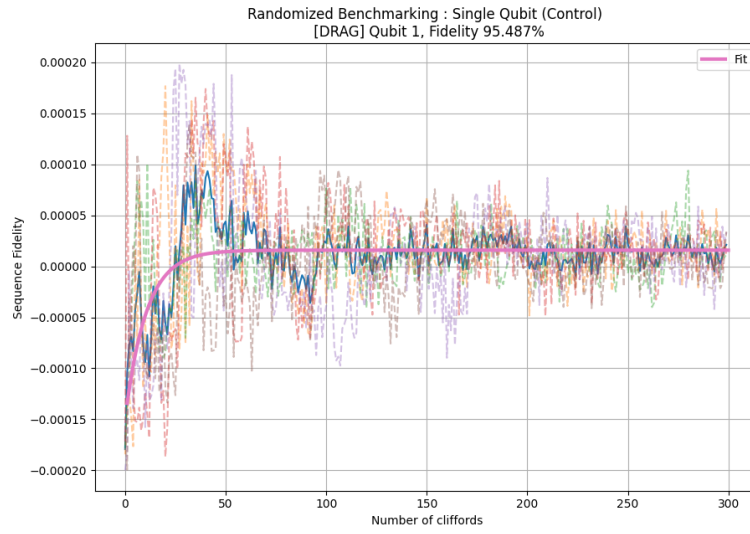
3.3.4 Automatic Amplitude Calibration

First, we take an initial guess (ansatz) for the pulse amplitudes of the 4 pulses (X_π , Y_π , $X_{\pi/2}$, $Y_{\pi/2}$) using the area scaling of power from the Time Rabi experiment, for a given pulse length. We define a configuration updater function that updates the configuration file with these initial amplitudes.

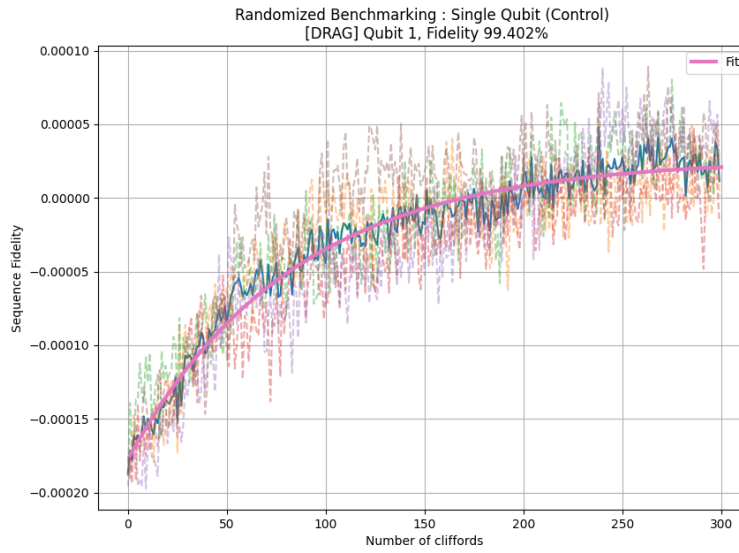
We bound our 4-tuple with $(\max(0, 0.5 * \text{amp}_i), \min(0.9, 2 * \text{amp}_i))$ to ensure that we do not exceed the capacities of our DAC. We then optimize the fidelity given by the ORBIT cost function, by updating the amplitude 4-tuple. Each iteration updates the configuration with the current 4-tuple and the ORBIT value as well as the parameter vectors are recorded. Once the Nelder-Mead optimization algorithm has concluded, we plot the parameter convergence and ORBIT infidelity.

3.3.5 ORBIT for DRAG and amplitude calibration

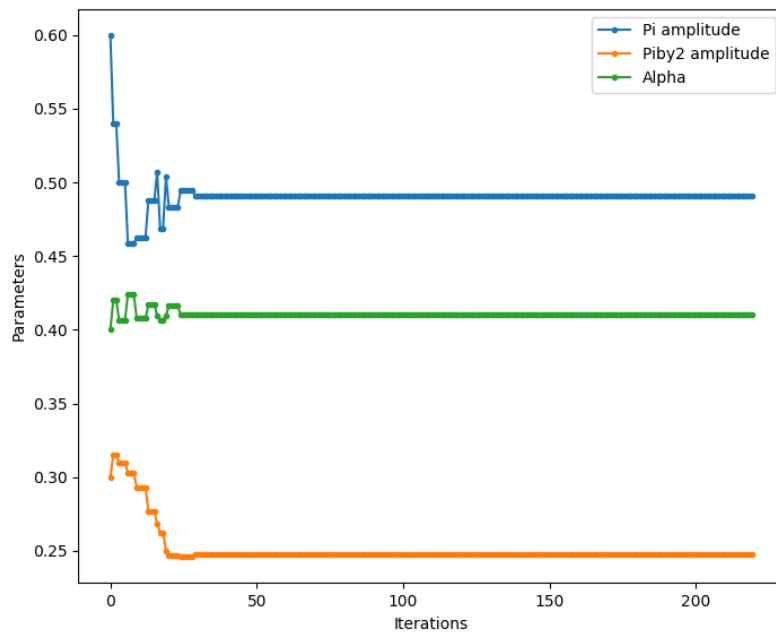
Now, if we consider DRAG corrections to the pulses as well, we have to calibrate the DRAG parameter as well. We consider a three-tuple parameter set of $\{\pi$ amplitude, $\frac{\pi}{2}$ amplitude, DRAG coefficient $\}$. Here, we use ORBIT as the figure-of-merit as RB is capable of indirectly measuring leakage errors. Specialized variants of leakage RB can also be modified to be used within ORBIT if the intention is to purely calibrate the DRAG parameter.



(A) Initial value of RB fidelity for guessed parameters.



(B) RB fidelity after optimization.



(C) Iterations to convergence of parameter values.

FIGURE 3.6: Closed-loop calibration using ORBIT.

3.4 Automated Single Qubit Tune-Up Protocol

In this section, we discuss the integrated automated tune-up protocol for fixed-frequency transmons. Each experiment here is scalable to parallel processing for all qubits in a Quantum Processing Unit (QPU). We also incorporate an efficient automated feedback cycle to correct for drifts in qubit frequency that might be incurred over a long time-scale operation. In effect, we are able to demonstrate cooldown to coherence in a completely autonomous protocol.

3.4.1 Results on a Tantalum Transmon

The protocol up to mixer calibration, time of flight calibration and readout resonator spectroscopy is as shown earlier.

1. **Autospectroscopy:** The broad sweep finds the qubit, but not the $\frac{0-2}{2}$ transition. It repeats till a high power and is still unable to find the $\frac{0-2}{2}$ transition, see Fig 3.7. Thus, it terminates with the mode of the global qubit frequency list taken as the qubit frequency (known to be at 5.34 GHz). Observe how the qubit peak has broadened in response to the increased power.

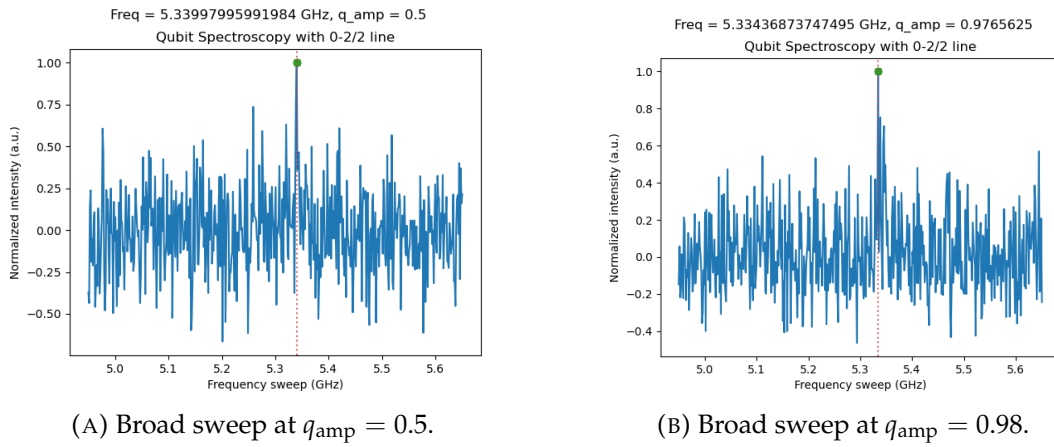


FIGURE 3.7: The broad sweep spectroscopy of the qubit.

We now move to the fine sweep around the broad sweep detected qubit frequency of 5.33 GHz. In Fig 3.8, observe how with narrower spans and lower power, the qubit peak can be reduced and the precision of the spectroscopy can be increased.

2. **Time Rabi:** The Time Rabi experiment is run, see Fig 3.9, and initial guesses for the pulse amplitudes of the 4-tuple $(X_{\pi}, Y_{\pi}, X_{\pi/2}, Y_{\pi/2})$ are determined using the determined Rabi frequency and amplitude scaled by a simple area power law to give the amplitudes necessary for our given pulse length.
3. **Time Ramsey:** The Time Ramsey interferometry experiment is run with a 20 KHz detuning, see Fig 3.10. The difference between the observed

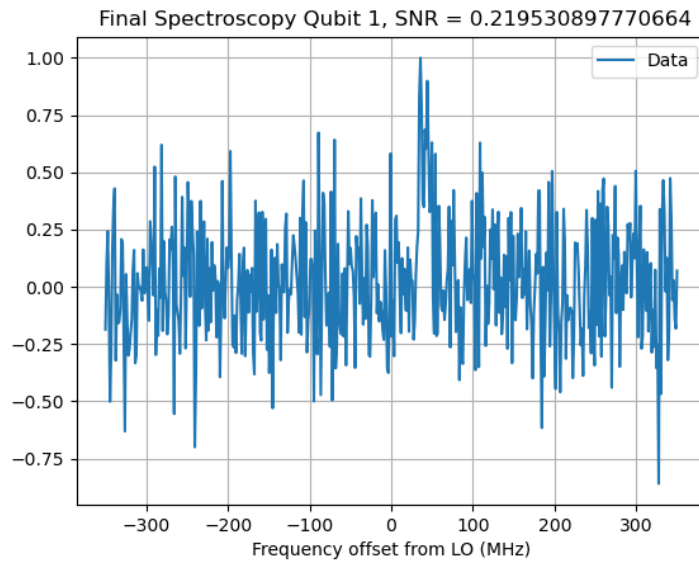
beating and the intentional detuning is added and subtracted to the qubit intermediate frequency $\omega_{q,IF}$ and the Ramsey experiment is re-run. The case in which the Ramsey fringe frequency is almost the detuning has the corrected qubit intermediate frequency.

4. **ORBIT Tune-up:** The 4-tuple of pulse amplitudes is now calibrated using the closed-loop ORBIT calibration. The amplitudes for each of the 4 pulses asymptotically converge to values that are distinct, even between X and Y pulses of the same rotation angle, as seen in Fig 3.11.
5. **Coherence:** The interleaved coherence experiment characterizing the T_1 , Ramsey and Echo time is run as shown in Fig 3.12a.
6. **Randomized Benchmarking:** The standard single-qubit Randomized Benchmarking experiment is run to gauge the fidelity of the 4-tuple of pulses tuned-up on the qubit, as shown in Fig 3.12b. This is at par with RB results from manually calibrated pulses.

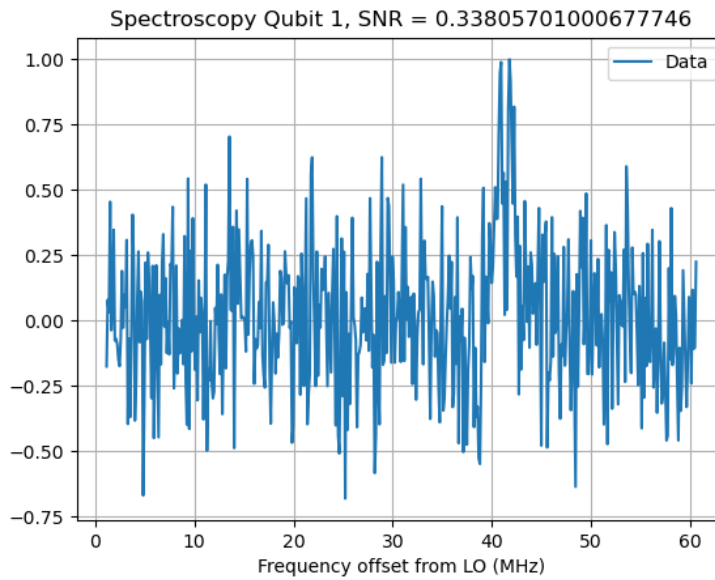
Note that this sample suffers from very poor readout SNR, particularly visible in the spectroscopy scans, but the protocol is still able to identify the qubit correctly and correctly calibrate pulses that achieve over 99% fidelity in Clifford-based randomized benchmarking. There is still scope to improve the performance of this qubit if the readout power and integration length is optimized, as an improvement in readout fidelity will have a cascading effect on virtually each experiment involved in this protocol.

The DRAG parameter was not calibrated in this experiment as the sample used restricted control to low powers, which subsequently meant longer pulse lengths. In this regime other error sources dominate, and the role of leakage error is diminished. However, it is a straightforward matter to include the DRAG calibration experiment after the ORBIT tune-up.

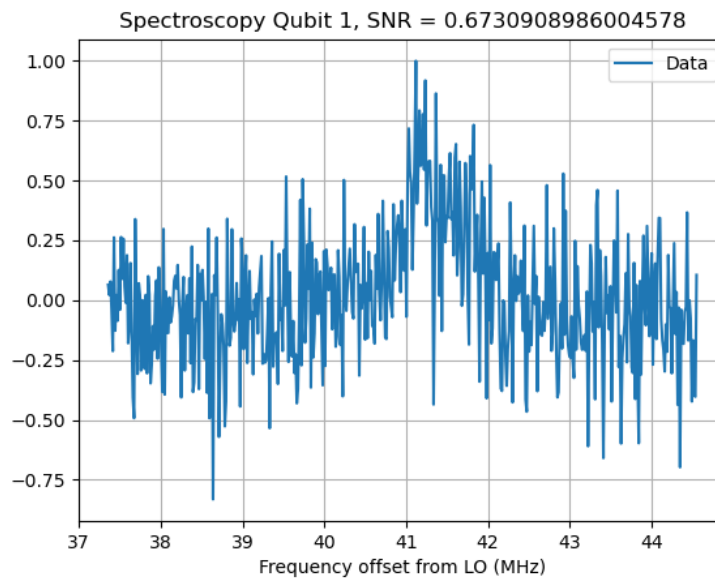
Further, a small feedback cycle can be set up which runs the Time Ramsey frequency correction and reoptimizes the pulse amplitudes and the DRAG parameter. This would be useful for maximizing the lifetime of a QPU when online, as correcting for drifts in qubit parameters can be done in an autonomous and automatic manner, without any human operator oversight.



(A) Fine qubit sweep with 700 MHz span.



(B) Fine qubit sweep with 60 MHz span.



(C) Fine qubit sweep with 7 MHz span.

FIGURE 3.8: The fine sweep spectroscopy of the qubit at lower powers and narrower spans.

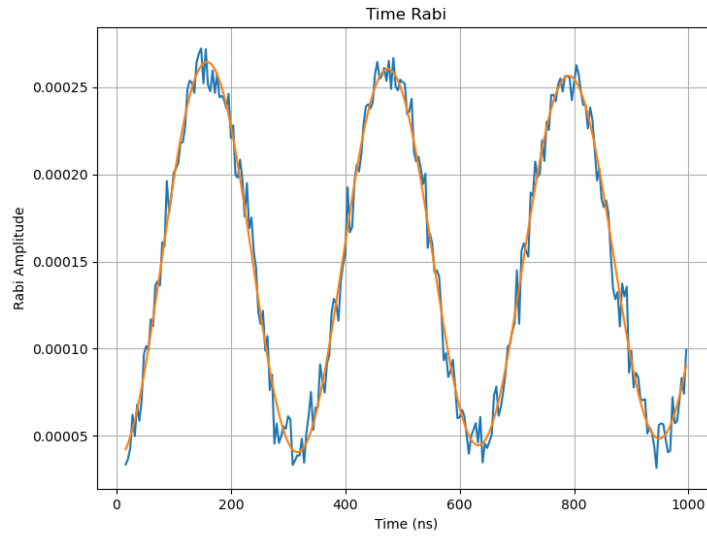
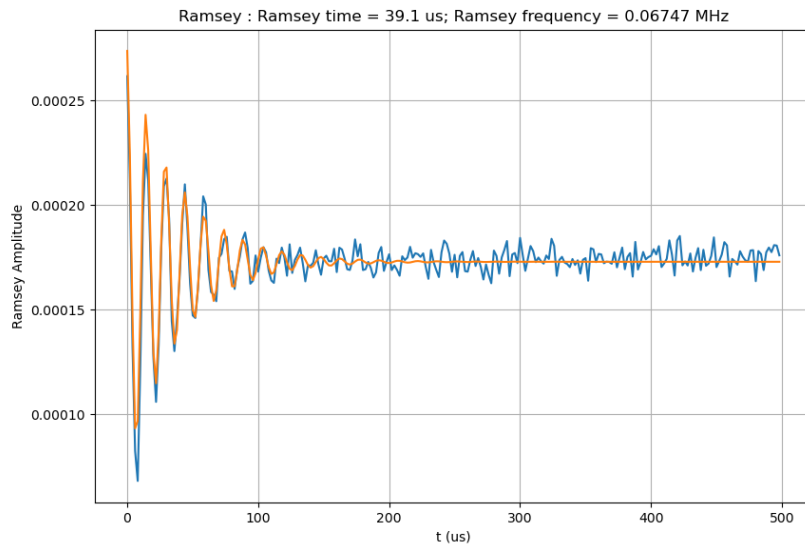
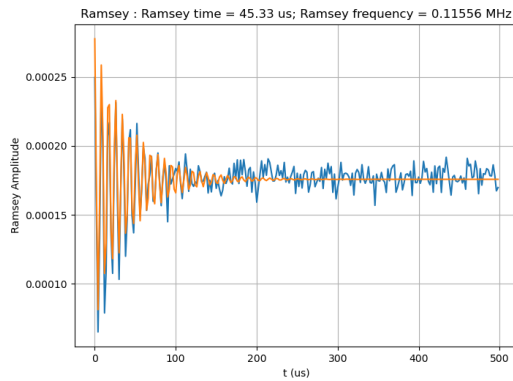
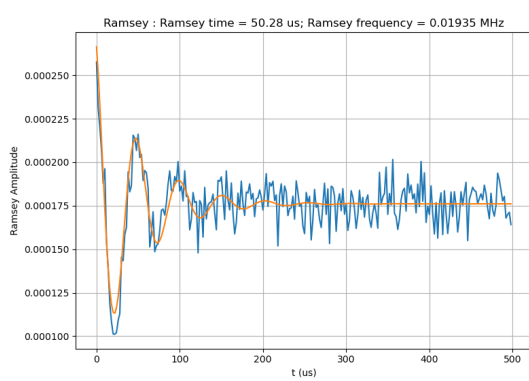


FIGURE 3.9: Time Rabi



(A) Ramsey with 20 KHz detuning shows beating.



(B) Ramsey with negatively biased qubit IF. (C) Ramsey with positively biased qubit IF.

FIGURE 3.10: Time Ramsey fine frequency correction.

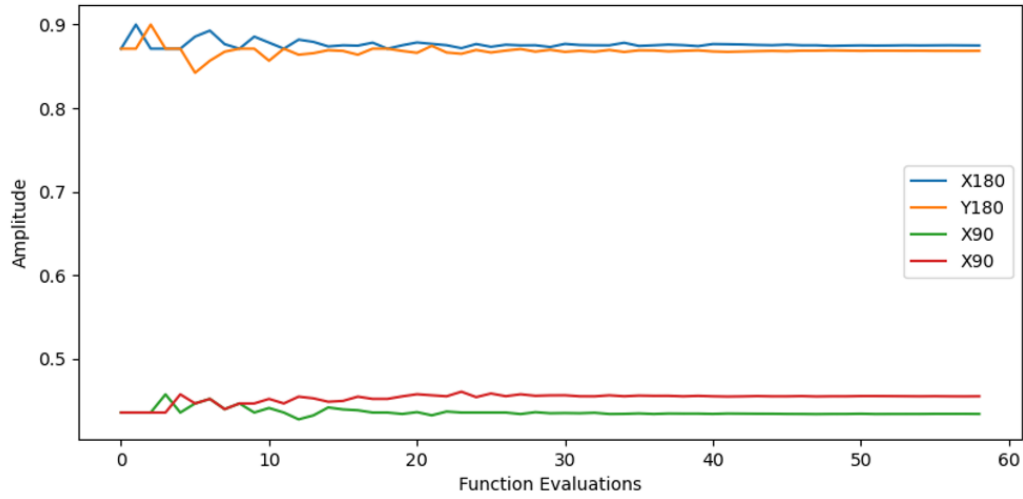
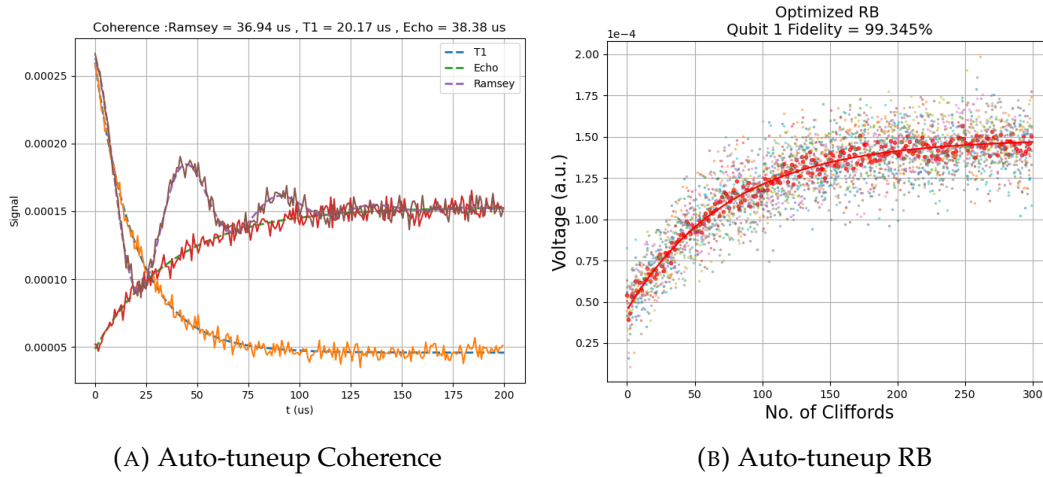


FIGURE 3.11: Pulse amplitude convergence using ORBIT



(A) Auto-tuneup Coherence

(B) Auto-tuneup RB

FIGURE 3.12: Auto-tuneup Coherence and RB after optimization.

4 Conclusion

4.1 A Brief Summary

This thesis has discussed the basic steps to tune up single qubit pulses right from spectroscopy to benchmarking. A new protocol to automate spectroscopy was introduced with the capability of handling spurious TLS lines, low SNR data and IQ calibration.

The DRAG method to address the prevalent leakage error was discussed and an experiment to calibrate the DRAG correction was shown. Further, a comparison was conducted to demonstrate the improvements offered by the DRAG correction even at relatively long pulse lengths of $50ns$.

The ALLXY and ORBIT methods were presented and discussed as feasible experimental figures of merit to characterize errors and enable closed-loop autonomous processor tune-up. Amplitude tune-up was automated to replace the time-consuming Power Rabi experiment using these techniques and single qubit DRAG as well as amplitude tune-up was also demonstrated.

In all, this thesis presents several crucial tools to enable automation and control of single-qubit gates and addresses key roadblocks in speeding up development. A solid foundation has been laid for multi-qubit tune-ups to now be attempted using these techniques.

4.2 Future Avenues

4.2.1 Multi-qubit operations

We would like to benchmark performance when multiple qubits are simultaneously driven for ORBIT, ALLXY and Coherence. This protocol is naturally scalable, but a rigorous understanding of the frequency shifts and leakage effects that could be incurred by simultaneous operation is needed.

4.2.2 Robust Single Qubit Pulses

We plan to introduce a new figure of merit which can quantify robustness based on a recent approach called Space Curve Quantum Control formalism (Nelson et al., 2023). By integrating an analytical error metric for robustness with our closed-loop ORBIT figure of merit, one can obtain single qubit pulses robust to detuning and ZZ error.

Bibliography

- Egger, D. J. and F. K. Wilhelm (June 2014). “Adaptive Hybrid Optimal Quantum Control for Imprecisely Characterized Systems”. In: *Physical Review Letters* 112.24, p. 240503. DOI: [10.1103/PhysRevLett.112.240503](https://doi.org/10.1103/PhysRevLett.112.240503). (Visited on 05/29/2023).
- Kelly, J. et al. (June 2014). “Optimal Quantum Control Using Randomized Benchmarking”. In: *Physical Review Letters* 112.24, p. 240504. DOI: [10.1103/PhysRevLett.112.240504](https://doi.org/10.1103/PhysRevLett.112.240504). (Visited on 05/29/2023).
- Krantz, P. et al. (June 2019). “A Quantum Engineer’s Guide to Superconducting Qubits”. In: *Applied Physics Reviews* 6.2, p. 021318. ISSN: 1931-9401. DOI: [10.1063/1.5089550](https://doi.org/10.1063/1.5089550). (Visited on 10/07/2023).
- Nelder, J. A. and R. Mead (Jan. 1965). “A Simplex Method for Function Minimization”. In: *The Computer Journal* 7.4, pp. 308–313. ISSN: 0010-4620. DOI: [10.1093/comjnl/7.4.308](https://doi.org/10.1093/comjnl/7.4.308). eprint: <https://academic.oup.com/comjnl/article-pdf/7/4/308/1013182/7-4-308.pdf>. URL: <https://doi.org/10.1093/comjnl/7.4.308>.
- Nelson, Hunter T. et al. (July 2023). “Designing Dynamically Corrected Gates Robust to Multiple Noise Sources Using Geometric Space Curves”. In: *Physical Review A* 108.1, p. 012407. DOI: [10.1103/PhysRevA.108.012407](https://doi.org/10.1103/PhysRevA.108.012407). (Visited on 11/12/2023).
- Reed, Matthew (2013). *Entanglement and Quantum Error Correction with Superconducting Qubits*. arXiv: [1311.6759](https://arxiv.org/abs/1311.6759) [quant-ph].